

GARROTXA COSMOLOGICAL SIMULATIONS OF MILKY WAY LIKE GALAXIES - I. HOT GAS AND THE MISSING BARYONS

SANTI ROCA-FÀBREGA¹, OCTAVIO VALENZUELA², PEDRO COLÍN³, FRANCESCA FIGUERAS¹, YAIR KRONGOLD² AND HÉCTOR VELÁZQUEZ⁴

¹ Departament d'Astronomia i Meteorologia and IEEC-UB, Institut de Ciències del Cosmos de la Universitat de Barcelona, Martí i Franquès, 1, E-08028 Barcelona.

² Instituto de Astronomía, Universidad Nacional Autónoma de México, A.P. 70-264, 04510, México, D.F.; Ciudad Universitaria, D.F., México.

³ Centro de Radioastronomía y Astrofísica, Universidad Nacional Autónoma de México, A.P. 72-3 (Xangari), Morelia, Michoacán 58089, México.

⁴ Instituto de Astronomía, Universidad Nacional Autónoma de México, A.P. 877, 22800, Ensenada, México.

Draft version December 3, 2024

ABSTRACT

We introduce a new set of simulations of a Milky Way like galaxy using the AMR code ART + hydrodynamics in a Λ CDM cosmogony. The simulation series is named GARROTXA and follow the formation of a late type galaxy from $z = 60$ with a final virial mass of $\sim 7.4 \times 10^{11} M_{\odot}$. This system has no major mergers since $z=3$ and at $z=0$ becomes a disk late-type spiral galaxy. Several of its large scale properties fall inside recent observational limits of our Galaxy, like the rotation curve shape, the presence of a stellar bar and flare, and a gaseous disk warp, as well as the stellar and baryonic mass. Here, as a first scientific exploitation of the model we study the total amount and spatial distribution of hot X-ray luminous gas. We do not observe in our models a significant presence of a hot gas thick disk as has been recently discussed in observational studies. The analysis of hot gas mock observations (column density and emission measure) revealed that commonly used hypothesis assumed to derive the total hot gas mass in the MW halo from observations lead to biases of about one order of magnitude. Our results suggest that such hot gas distribution is highly anisotropic and that its total mass can account for a non-negligible portion of the missing cosmic baryons leaving still open the contribution of circumgalactic gas. Finally, we have found a clear correlation between the total hot gas mass and the dark matter halo mass of galactic systems. If confirmed, this correlation can become a new method to constrain the total mass of galaxies, in particular the one of the Milky Way.

Keywords: galaxies:formation - methods:numerical - Galaxy: halo

1. INTRODUCTION

One of the most challenging problems in Λ CDM cosmological simulations in recent years has been to obtain realistic Milky Way (MW) like systems with extended disks, star formation rates and baryonic fractions that are in agreement with observations.

It was long known that disks form when the gas cools and condenses within the dark matter halos (White & Rees 1978; Fall & Efstathiou 1980; Mo et al. 1998) conserving the angular momentum obtained through external torques from neighbouring structures (Hoyle 1953; Peebles 1969). An important problem that arose from the first numerical simulations was the lack of angular momentum in disks after the collapse (Navarro & Benz 1991; Navarro & Steinmetz 2000). This angular momentum problem drive to galactic disks too small and dominated by big and massive bulges. Regardless of such challenges, important progress about galaxy assembly was achieved (Abadi et al. 2003). Two major drawbacks were found to be the responsible of this problem. First, artificial losses of angular momentum caused by insufficient resolutions and other numerical effects (Okamoto et al. 2003; Governato et al. 2004; Kaufmann et al. 2007). Second, the dynamical friction that transfers the orbital angular momentum of merging substructures to the outer halo and causes cold baryons to sink to the center of the proto-galaxy being consumed

at early ages in the formation of an old spheroid rather than being available for the formation of a disk, at latter ages (e.g. Maller & Dekel 2002).

More recently, the attempts for obtaining realistic disk galaxies in a Λ CDM universe succeeded as can be seen in Robertson et al. (2004); Okamoto et al. (2005); Governato et al. (2004). In these simulations the authors used the so called zoom technique to produce individual galactic systems with a high resolution inside cosmological simulations with much less resolution. The authors selected halos with masses similar to the ones of the MW, and with a quiet merger histories in the last stages of the simulation to be resimulated with higher resolution.

Several improvements accounted for the recent relative success of these models on forming disk galaxies: better numerical resolutions, the implementation of an efficient supernovae (SNe) feedback (Stinson et al. 2006) and new star formation and evolution recipes. These new physical processes implemented in the codes prevent efficient gas cooling and condensation and remove low-angular-momentum material from the central part of galaxies (Brook et al. 2012) making galaxies to follow observed scaling relations like the Tully-Fisher for the first time (Governato et al. 2007) and relaxing some tension related between observations and Λ CDM predictions (Governato et al. 2010). However, although they obtained realistic disk galaxies none of them was

able to produce viable MW-like late type spiral. In the recent years authors like Scannapieco et al. (2009); Stinson et al. (2010); Piontek & Steinmetz (2011); Agertz et al. (2011); Brooks et al. (2011); Feldmann et al. (2011); Guedes et al. (2011) obtained realistic rotationally supported disks with properties closely resembling the MW one. In these models gas is acquired through filamentary cold flows that was never shock-heated to the halo virial temperature (Kereš et al. 2005; Dekel et al. 2009). This cold gas is the fuel for the late star formation in disks (Kereš et al. 2009; Ceverino et al. 2010).

However most of these works obtained systems with too peaked rotation curves in the center. Agertz et al. (2011) showed that some key parameters to avoid the formation of these peaked systems are the star formation efficiency or the gas density star formation threshold. They argued that to use proper values for these parameters is necessary to reproduce the subgrid physics of star formation in molecular clouds. A combination of both parameters allow the system to consume the gas in the star formation region fast enough to ensure that the energy provided by SNe is not radiated too fast by the gas cooling. This too efficient cooling is known as 'overcooling problem' and initially was solved by stopping the cooling in the star formation region for several Myr after star formation (Stinson et al. 2006; Governato et al. 2007). In more recent high resolution simulations this effect has been naturally included by adding new physical processes like radiation pressure from massive stars (Krumholz 2015) or early feedback (Stinson et al. 2013) and currently the need of such effect is widely acknowledged but the physical nature is still a challenge (Oman et al. 2015; González-Samaniego et al. 2014).

Obtaining realistic MW-like systems open several possibilities on the study of galaxy formation and evolution. Here, we introduce a set of new high resolution MW like systems with extended disks and unpeaked slowly decreasing rotation curves. The models presented here reach similar or better levels of realism than the most recent works in the field (Guedes et al. 2011; Bird et al. 2013; Mollitor et al. 2014) but using a different code and slightly better spatial resolution (109 pc).

In the galaxy formation and evolution processes it is interesting to study the generation of galactic hot gas halo coronas and their properties. The presence of these hot halo coronas in dark matter halos was a natural prediction from structure formation models (White & Rees 1978; White & Frenk 1991). From the point of view of large volume hydrodynamical galaxy formation simulations, some attempts have been made in order to investigate the presence and detectability of such hot halo corona. Toft et al. (2002) presented one of the first studies towards this direction, however due to the inefficient feedback, the amount of hot gas in their simulated halo was too small. Global properties of hot gas halo corona in MW-like simulations have also been studied (e.g. Guedes et al. 2011; Mollitor et al. 2014). Most recently, models that account for the SNe feedback and implement new star formation processes, succeeded in obtaining more realistic results when compared with observations (Crain et al. 2010, 2013).

From an observational point of view the hot gas

halo corona was proposed to be detected by its X-ray emission. First detections were done by Forman et al. (1985) in external galaxies and later on several authors get better detections in other systems and studied them deeper (e.g. Mathews & Brighenti 2003; Li et al. 2008; Anderson & Bregman 2010; Bogdán & Gilfanov 2011). More recently, using Chandra, XMM-Newton, FUSE and other instruments it was detected a large reservoir of this hot gas surrounding our galaxy and it was proposed that it could account for a fraction of the so called missing baryons mass. These detections were done by the analysis of X-ray absorption lines from OVII and OVIII which only exist in environments with temperatures between 10^6 and 10^7 K, the MW halo has a temperature of about $\log T = 6.1-6.4$ (Yao & Wang 2007; Hagihara et al. 2010). The problem of using this technique is that these X-ray absorption lines only can be observed in the directions of extragalactic luminous sources (QSO, AGN, ...) or galactic X-ray emitters as X-ray binaries. This observational strategy gives a limited information about hot gas distribution and position, inside the galactic halo or in the intergalactic medium. Using this limited information, several recent works (Gupta et al. 2012; Miller & Bregman 2013; Gupta et al. 2014) obtained a value for the total hot gas mass embedded in the galactic halo that accounts for about 10-50% of missing baryons. To obtain these total hot gas mass from the low number of available observations the authors needed to assume a simple hot gas density profile. It is important to be aware that this assumption can lead to total hot gas mass values dominated by errors.

In our simulations we have obtained values for the total hot gas mass that are of the order of the one observed in the MW. Such models allow us to determine its distribution in a full sky view and to find observational biases when using a small number of line of sight observations to compute total mass, if they exist. We are also allowed to study the origin of the observed hot gas distribution, although the feedback and star formation recipes used are critical to determine the final configurations. Using our simulations we also studied how the hot gas component embedded in the DM halo can account for part of the missing baryons in galaxies. The missing baryons problem arose when the analysis of high precision data obtained by WMAP and Planck pointed to that the amount of baryons in stars, cold gas and dust components does not agree with what is predicted (e.g. Hoekstra et al. 2005; McGaugh et al. 2007). The cosmic ratio Ω_b/Ω_M is 3-10 times larger than the one observed for galaxies. To solve this missing baryons problem several authors proposed that galactic winds, SNe feedback or strong AGN winds ejected part of the galactic baryons to the circumgalactic medium (CGM) as hot gas. Others proposed that most of the gas never collapsed into the dark matter halos as it was previously heated by SNe of Population III.

This paper is laid out as follows. In Sec. 2 we present the code and initial conditions we have used. In Sec. 3 we introduce the general properties of our MW-like simulations, whilst in Sec. 4 we present the study of their hot gas component. We summarize our conclusions in Sec. 5.

2. GARROTXA SIMULATION

2.1. *The code*

The numerical simulations we introduce in this work (GARROTXA: Galaxy high Resolution Runs in a cosmological Context using ART) have been computed using the Eulerian hydrodynamics + N-body ART code (Kravtsov et al. 1997; Kravtsov 2003). This is the Fortran version of the code introduced in Colín et al. (2010) in the context of the formation of low-mass galaxies. This version differs from the one used by Ceverino & Klypin (2009), among other things, in the feedback recipe; unlike them, we deposit *all* the energy coming from stellar winds and supernovae in the gas *immediately after* the birth of the stellar particle. This sudden injection of energy is able to raise the temperature of the gas in the cell to around 10^7 K, high enough to make the cooling time larger than the crossing time and thus avoiding most of the overcooling. Here we have used it to obtain high resolution Milky Way like (MW-like) galaxies.

The code is based on the adaptive mesh refinement technique what allows to increase the resolution selectively in a specified region of interest around a selected dark matter halo. The physical processes included in this code are the cooling of the gas and its subsequent conversion into stars, the thermal stellar feedback, the self-consistent advection of metals, and a UV heating background source. The cooling and heating rates incorporate Compton heating/cooling, atomic, and molecular hydrogen and metal-line cooling, UV heating from a cosmological background radiation (Haardt & Madau 1996), and are tabulated for a temperature range of 10^2 K $<$ T $<$ 10^9 K and a grid of densities, metallicities (from $[M/H] = -3.0$ to $[M/H]=1.0$, in solar units), and redshifts, using the CLOUDY code (Ferland et al. 1998, version 96b4).

The star formation (SF) is modeled as taking place in the coldest and densest collapsed regions, defined by $T < T_{SF}$ and $n_g > n_{SF}$, where T and n_g are the temperature and number density of gas, respectively, and T_{SF} and n_{SF} are the temperature and density SF threshold, respectively. A stellar particle of mass m is placed in all grid cells where these conditions are simultaneously satisfied, and this mass is removed from the gas mass in the cell. The particle subsequently follows N-body dynamics. No other criteria are imposed. In most of the simulations presented here, the stellar particle mass, m, is calculated by assuming that a given fraction (SF local efficiency factor ϵ_{SF}) of the cell gas mass, m_g , is converted into stars; that is, $m = \epsilon_{SF} m_g$, where ϵ_{SF} is treated as a free parameter. In MW-like models presented here we have used $\epsilon_{SF} = 0.65$, $T_{SF} = 9000$ K and $n_{SF} = 1$ cm $^{-3}$, where this last is the density threshold in hydrogen atoms per cubic centimeter. These values have shown to successfully reproduce a galaxy rotation curve similar to the one of the Milky Way at $z=0$. These values let the thermal feedback to be efficient in regions of dense, cold, star-forming gas and they are not as large as to imply that most of the cell gas is exhausted. Since stellar particle masses are much more massive than the mass of a star, typically $10^4 - 10^5 M_\odot$, once formed, each stellar particle is considered as a single stellar population, within which

the individual stellar masses are distributed according to the Miller & Scalo (1979) IMF. Stellar particles eject metals and thermal energy through stellar winds and Type II and Ia SNe explosions. Each star more massive than $8 M_\odot$ is assumed to dump into the ISM, instantaneously, 2×10^{51} erg of thermal energy; 10^{51} erg comes from the stellar wind, and the other 10^{51} erg from the SN explosion. Moreover, the star is assumed to eject $1.3 M_\odot$ of metals. For the assumed Miller & Scalo (1979) initial mass function, IMF, a stellar particle of $10^5 M_\odot$ produces 749 Type II SNe. For a more detailed discussion of the processes implemented in the code, see Kravtsov (2003); Kravtsov et al. (2005). Stellar particles dump energy in the form of heat to the cells in which they are born. If sub-grid physics are not properly simulated, most of this thermal energy, inside the cell, is radiated away. Thus, to allow for outflows, it is common to adopt the strategy of turning off the cooling during a time t_{off} in the cells where young stellar particles (age $< t_{off}$) are placed (see Colín et al. 2010). This mechanism along with a relatively high value of ϵ_{SF} allow the gas to expand and move away from the star-forming region. As t_{off} can be linked to the crossing time in the cell at the finest grid, we could see this parameter as depending on resolution in the sense that the higher the resolution, the smaller its value. In simulations presented here the cooling is stopped for 40 Myr. Although it has been demonstrated that for spatial resolutions similar to the ones in our models this process is unnecessary when simulating dwarf galactic systems, a more detailed study is necessary to ensure that the same occurs when simulating MW-like galaxies.

2.2. *Simulation technique and halo selection*

The simulations presented here have been run in a Λ CDM cosmology with $\Omega_0 = 0.3$, $\Omega_\Lambda = 0.7$, $\Omega_b = 0.045$, and $h = 0.7$. The CDM power spectrum was taken from Klypin & Holtzman (1997) and it was normalized to $\sigma_8 = 0.8$, where σ_8 is the rms amplitude of mass fluctuations in 8 Mpc h^{-1} spheres. To maximize resolution efficiency, we used the zoom-in technique. First, a low-resolution cosmological simulation with only dark matter (DM) particles was ran, and then regions of interest (DM halos) were picked up to be re-simulated with high resolution and with the physics of the gas included. The low-resolution simulation was run with 128^3 particles inside a box of 20 Mpc h^{-1} per side, with the box initially covered by a mesh of 128^3 cells (zeroth level cells). At $z=0$, we searched for MW-like mass halos ($7.0 \times 10^{11} M_\odot \leq M_{vir} \leq 1.5 \times 10^{12} M_\odot$) that was not contained within larger halos (distinct halos). We selected only halos that have had not major mergers since $z=1.5$ and that at $z=0$ have not a similar mass companion inside a sphere of 1 Mpc. Other restrictions we have imposed are that halos need to be in a filament or a wall not in a void or a knot, and far from cosmological box borders. After this selection, a Lagrangian region of $3 R_{vir}$ was identified at $z=60$ and re-sampled with additional small-scale modes (Klypin et al. 2002). The virial radius in the low resolution runs, R_{vir} , is defined as the radius that encloses a mean density equal to Δ_{vir} times the mean density of the universe, where

Δ_{vir} is a quantity that depends on Ω_0 , Ω_Λ , and z . For example, for our cosmology $\Delta_{vir}(z=0) = 338$ and $\Delta_{vir}(z=1) = 203$. The number of DM particles in the high resolution region depends on the number of DM species and the mass of the halo. For models with four or five species this value varies from $\sim 1.5 \times 10^6$ (model GARROTXA242) to about 7.0×10^6 (model GARROTXA321). The corresponding DM mass per particle of model galaxies (m_{dm}) is given in Tab. 1.

In ART, the initially uniform grid is refined recursively as the matter distribution evolves. The cell is refined when the mass in DM particles exceeds $81.92 (1 - F_{b,U}) m_p / f_{DM}$ or when the mass in gas is higher than $81.92 F_{b,U} m_p / f_g$, where $F_{b,U}$ is the universal baryon fraction, $m_p = 7.75 \times 10^4 M_\odot h^{-1}$ is the mass of the lightest particle specie in the DM only simulation, and f_{DM} and f_g are factors that control the refinement aggressivity in the dark matter and gas components, respectively. In our models $F_{b,U} = 0.15$ according to the cosmology we have imposed and the mean DM and gas densities in the box are assumed to be equal to the corresponding universal averages. For the simulations presented in this work the grid is always unconditionally refined to the fourth level, corresponding to an effective resolution of 2048^3 DM particles. A limit also exists for the maximum allowed refinement level and it is what will give us the spatial size of the finest grid cells. Here we allow the refinement to go up to the 11 refinement level what corresponds to a spatial size of the finest grid cells of 109 comoving pc. Our main model is a re-simulation of a MW-like halo of $M_{vir} \sim 7.4 \times 10^{11} M_\odot$. However we also re-simulated other halos with masses in between $13.9 \times 10^{11} M_\odot$ and $2.0 \times 10^{11} M_\odot$. We have used these simulations to find how the general properties of the galactic system change with mass. For each one of these models we have also made simulations changing initial parameters such as ϵ_{SF} , n_{SF} , resolution or number of DM species. This set of models helps us to assess how the final results depend on the initial conditions. A more detailed study of the effects of changing the simulation parameters can be find in González-Samaniego et al. (2014). Tab. 1 summarizes the properties of the main MW-like simulations presented here.

Although our MW-like simulations are very realistic, some physical processes are not well implemented in the code we have used. For instance, the AGN feedback, the molecular H_2 clouds, a deep chemical treatment, the radiation pressure or the photoionization from massive stars. However, the last two are now implemented in a new version of the code.

In this work we study MW-like systems, however it is not our goal to reproduce all observed properties. Here we define a MW-like system as the one that has a total mass, v_{max} and disk with similar mass and scale lengths as the ones observed. Such system has to be placed in a filament or wall, with no massive halos nearby and has to have had a quiescent recent assembling history. These kind of systems will be our main MW-like models. Details of each realization will depend on selected subgrid physical parameters, environment and assembling histo-

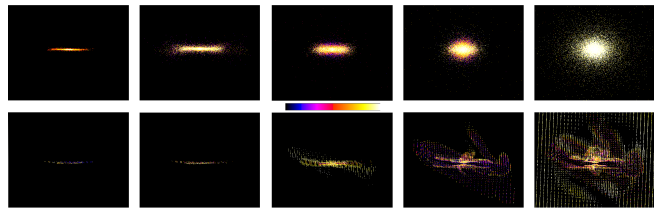


Figure 1. Edge on (first two rows) and face on view (last two rows) of stars and gas density in our simulated Milky Way sized galaxy. Each column correspond to a different stellar age and gas temperature, respectively. From left to the right, 0–4 Gyr / 250–1000 K, 4–9 Gyr / 1000–5000 K, 9–10 Gyr / 5000– 10^4 K, 10–11 Gyr / 10^4 – 10^5 K, 11–13.467 Gyr / 10^5 – 10^6 K. All panels span 46 kpc in the vertical direction and 58 kpc in the horizontal. Color code indicates stellar age or gas temperature from the minimum (black) to the maximum (white).

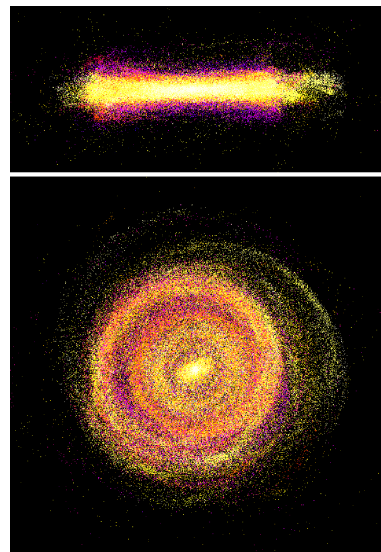


Figure 2. Edge on (top) and face on (bottom) views of a young stellar population (0–7 Gyr) of model GARROTXA323 at $z=0$. Both Panels span 50 kpc in the x-axis. The y-axis span 22 kpc in the top panel and 50 kpc in the bottom. Color code indicates stellar age, qualitatively.

ries.

3. RESULTS

3.1. General properties of MW-like model realizations

In this work we focus mostly in three MW-like models that differ only in the aggressivity on the refinement criteria. These models are the ones we have found to be in a better agreement with observed properties of the MW. The spatial resolution of all our models is high, around 109 pc. Model GARROTXA321 is the one with

a lightest refinement, GARROTXA322 has intermediate conditions and GARROTXA323 is the one with hardest refinement conditions (harder means that the code uses a lower mass threshold for the refinement). All parameters we present in this section are summarised and compared with recent MW-like models and with its observational values in Tab. 1.

3.1.1. Morphology

At $z \sim 0$ our three models are late type massive spiral galaxies with several non-axisymmetric structures in the disk such as bars or spirals (see Fig. 1 and 2). Their assembling history is quiet after $z=1.5$ and the last major merger occurs at $z=3$. In Fig. 1 we show the edge on (first two rows) and face on (last two rows) views of stars and gas density of our model GARROTXA321 at $z=0$. For the other two models the main picture is similar but with a larger number of stellar particles. Each column correspond to a different stellar age and gas temperature, respectively (see figure caption). In this figure it can be observed that young stellar component (0–4 Gyr) is distributed in a flat disk structure. On the other hand, older stellar populations (4–10 Gyr) are also distributed into a disk structure but in these cases not as flat as the younger. We argue that disk scale height and length depends on the age of the stellar population and that the former is higher and the latter is smaller when the population gets older, this issue will be addressed in Sec. 3.4.2. Another interesting property that can be easily observed in the edge on views of our models is that stellar population has an evident flare that is more evident for older populations. The face on view of the younger stellar population shows the presence of rings, spiral arms and also a young bar, in the disk. Spirals, rings and the young bar can be better observed in models GARROTXA322 and GARROTXA323 where the number of stellar particles is higher (see Fig. 2). The young bar has grown from disk particles that have ages between 0 and 8–9 Gyr. The old stellar population (11–13.476 Gyr) is distributed in a bar/ellipsoid component and it has been originated in the last major merger at $z=3$ (Valenzuela et al. in preparation). Finally, the gas component is distributed in different regions of the system depending on its temperature: cold gas is present in the young stellar disk region and hot gas fills the out-of-plane region and is embedded in the DM halo. It is also interesting to see how cold/intermediate gas has a warped structure that is also marginally observed in the stellar component.

3.1.2. Stellar, gas and dark matter virial mass

Here we define the virial radius (r_{vir}) as the one where the sphere of radius r_{vir} encloses a mean density 97 times denser than the critical density (ρ_{crit}) of a spatially flat Universe $\rho_{crit}=3H^2(z)/(8\pi G)$. We have used value 97 as it is the value derived from the spherical top-hat collapse model for Λ CDM at $z=0$ for our cosmology (Bryan & Norman 1998). This virial radius definition is borrowed from structure growth theory and then its use is not appropriated when one wants to define a physically meaningful halo edge (Cuesta et al. 2008; Zemp 2013). To avoid this problem we also give the properties for another commonly used definition

which is r_{200} , the radius that encloses a mean density equal to 200 times ρ_{crit} . Using the first definition we have obtained that the virial radius at $z=0$ is $r_{vir} \sim 230$ kpc in all our three models and that the mass enclosed in this radius is $M_{vir}=7.20-7.61 \times 10^{11} M_{\odot}$. This value for the M_{vir} falls well inside the observational range that is $M_{vir}=0.6-2.4 \times 10^{12} M_{\odot}$ by Xue et al. (2008), Kafle et al. (2012), Boylan-Kolchin et al. (2013) and Kafle et al. (2014). The total mass enclosed at $r_{200}=175.6$ kpc is $M_{200}=6.71-6.90 \times 10^{11} M_{\odot}$. Total virial mass is distributed in dark, stellar and gaseous matter as follows: $M_{DM}=5.86-6.79 \times 10^{11} M_{\odot}$, $M_{*}=6.1-6.2 \times 10^{10} M_{\odot}$ and $M_{gas}=1.73-2.70 \times 10^{10} M_{\odot}$. The baryonic fraction of our models is $F_{b,U}=0.104-0.121$. These values are 19–31% smaller than the universal value for the adopted cosmology which is $F_{b,U}=0.15$. Inside r_{vir} , and for the model GARROTXA321, we have a total number of particles of $N_{total}=7.52 \times 10^6$, where $N_{DM1sp}=7.12 \times 10^6$ and $N_{*}=3.94 \times 10^5$ and a total number of gas cells of 2.0×10^6 . For models with a more aggressive refinement the number of stellar particles and gas cells grow up to 2.34×10^6 and 6.8×10^6 , respectively. All dark matter particles inside virial radius belong to less massive DM specie and have a mass of $9.25 \times 10^4 M_{\odot}$. Star particles have masses between $\sim 10^3$ and $1.2 \times 10^6 M_{\odot}$. All these parameters are summarized in Tab. 1.

3.1.3. Circular velocity curves

Circular velocity curves of our main simulations, computed using the $\sqrt{GM_{<r}/r}$ approach, are shown in black at Fig. 3 top left panel. Circular velocity curves have also been computed using the real galactic potential by using Topsy package. Results obtained using both techniques are in good agreement. We also show circular velocity curves from other state of the art MW-like simulations: Klypin et al. (2002) B1 model (blue), Mollitor et al. (2014) model (magenta), Guedes et al. (2011) ERIS simulation (green). As a comparison we show in red the analytical fit to the Sofue et al. (2009) MW rotation curve data, presented in Pichardo et al. (2003). As solid lines we show total circular velocity curve while the DM, stellar and gas components are shown as long dashed, dotted and short dashed lines, respectively. In the top right panel we show GARROTXA321 velocity rotation curves of stars and gas, computed as the mean of the tangential velocity in rings centered to the galactic center (cyan solid and dashed lines), and the total circular velocity curve obtained using $V_c=\sqrt{GM_{<r}/r}$ approach. As expected, gas follows the circular velocity while stars are affected by the asymmetric drift. We also compare stellar rotation curve of our simulation (cyan solid line) with values from MW observations. We show rotation velocity curve estimations from blue horizontal-branch halo stars in the SDSS (Xue et al. 2008) (cyan and magenta dots), from Sofue et al. (2009) (red dots) and from observations of López-Corredoira (2014) (green dots). In the bottom panel we compare the recent data for the circular velocity curve obtained by Reid et al. (2014), using high mass star forming regions, with the total circular velocity curve of our GARROTXA321 model. As can be seen in the figure our models are in a very good agreement with the most recent observational data. We

also show the recent hypothetical gaseous rotation curve of the Milky Way obtained by Chemin et al. (2015) after correcting for bar non-circular motions. It is important to mention that we only show results for GARROTXA321 model because circular velocity curves of models GARROTXA322 and GARROTXA323 do not differ significantly. The peak of $z=0$ circular velocity of our models is reached at $R_{peak} \sim 5.69$ kpc with a value of $V_c(R_{peak})=237.5-243.8$ km s $^{-1}$, the value at a standard solar radius ($R_{\odot}=8$ kpc) is $V_{c\odot}=233.3-239.8$ km s $^{-1}$. Also the ratio between circular velocity at 2.2 times disk scale radius ($V_{2.2}$) and circular velocity at r_{200} (V_{200}) of our simulations ($V_{2.2}/V_{200} \sim 1.9$ km s $^{-1}$) is well inside the observational range for the MW that is $1.67^{+0.31}_{-0.24}$ km s $^{-1} - 1.11^{+0.22}_{-0.20}$ km s $^{-1}$ (Xue et al. 2008; Dutton et al. 2010).

An interesting exercise has been to compare circular velocity curves of our simulations with the one of Guedes et al. (2011) model. We have easily seen that our simulations have a bit higher velocity curves and do not present a peak in the inner regions as in Guedes et al. (2011). In simulations this internal peak is usually associated with the presence of a massive bulge in the central parts of the simulated galactic system. On the other hand, a similar peak in the V_c is shown in observational work of Sofue et al. (2009). It is in discussion whereas this peak detected in Sofue et al. (2009) observations is a signature of non-circular motions inside the bar or of a massive bulge (Duval & Athanassoula 1983; Chemin et al. 2015). Non-circular motions need to be computed to solve such question. We plan to undertake this work in a near future following the one started by Chemin et al. (2015).

Finally, despite of the rotation and circular velocity curves we introduce here fall well inside observational ranges it is important to take into account that nowadays observational uncertainties are still high.

	r_{vir} [kpc]	M_{vir} [M_{\odot}]	M_{*} [M_{\odot}]	M_{gas} [M_{\odot}]	M_{hotgas} [M_{\odot}]	$M_{warmgas}$ [M_{\odot}]	$M_{coldgas}$ [M_{\odot}]
G.321	230.1	7.33×10^{11}	6.1×10^{10}	2.70×10^{10}	1.22×10^{10}	5.66×10^9	9.34×10^9
G.322	230.1	7.20×10^{11}	6.1×10^{10}	1.73×10^{10}	0.98×10^{10}	5.98×10^9	1.52×10^9
G.323	230.1	7.61×10^{11}	6.2×10^{10}	1.96×10^{10}	1.32×10^{10}	4.54×10^9	1.86×10^9
ERIS	239.0	7.90×10^{11}	3.9×10^{10}	5.69×10^{10}	3.60×10^{10}	14.20×10^9	6.70×10^9
MollitorB	234.0	7.10×10^{11}	5.6×10^{10}	7.96×10^{10}	—	—	—
MW obs.	—	$1.0 \pm 0.30 \times 10^{12}$	$4.9\text{--}5.5 \times 10^{10}$	—	—	—	$7.3\text{--}9.5 \times 10^9$
	r_{200} [kpc]	M_{200} [M_{\odot}]	$F_{b,U}$	m_{DM1sp} [M_{\odot}]	m_{*min} [M_{\odot}]	m_{*max} [M_{\odot}]	m_{SPH} [M_{\odot}]
G.321	175.6	6.84×10^{11}	0.120	0.93×10^5	0.24×10^4	120.0×10^4	—
G.322	175.6	6.71×10^{11}	0.109	0.93×10^5	0.12×10^4	120.0×10^4	—
G.323	175.6	6.90×10^{11}	0.107	0.93×10^5	0.12×10^4	120.0×10^4	—
ERIS	175.0	6.60×10^{11}	0.120	0.98×10^5	0.63×10^4	0.63×10^4	2.0×10^4
MollitorB	176.5	6.28×10^{11}	0.191	2.30×10^5	4.50×10^4	4.50×10^4	—
MW obs.	—	—	—	—	—	—	—
	N_{part} [10^6]	N_{DM1sp} [10^6]	N_{*} [10^6]	N_{gas} [10^6]	Resolution [pc]	CPU time [10^4 h]	CODE
G.321	7.52	7.12	0.39	2.0	109(1cell)	2.5	ART + hydro
G.322	7.95	7.08	0.86	5.0	109(1cell)	4.3	ART + hydro
G.323	9.44	7.10	2.34	6.80	109(1cell)	9.2	ART + hydro
ERIS	15.60 (+SPH)	7.00	8.60	3.0	120(ϵ)	160.0	GASOLINE (SPH)
MollitorB	6.06	3.91	2.15	2.50	150(1cell)	—	RAMSES (hydro)
MW obs.	—	—	$\sim 10^{11}$	—	—	—	—
	$c=r_{vir}/r_s$	R_d [kpc]	$h_{z,young}$ [pc]	$h_{z,old}$ [pc]	M_{hotgas}/M_{vir}	α	SFR ($z=0$) [$M_{\odot} \text{ yr}^{-1}$]
G.321	28.5	2.56 (4.89/2.21)	277 (exp)	1356	0.016	-0.62	0.27
G.322	26.8	3.20 (5.26/2.26)	295 (exp)	960	0.013	-0.83	0.02
G.323	26.9	3.03 (3.19/3.31)	393 (exp)	1048	0.017	-0.67	0.32
ERIS	22.0	2.50	490 (sech ²)	—	0.017	-1.13	1.10
MollitorB	56.5	3.39	—	—	0.046	4.54	4.75
MW obs.	$21.1^{+14.8}_{-8.3}$	2.0–4.5	300±60	600–1100±60	—	—	0.68–1.45
	$V_{c\odot}(R=8 \text{ kpc})$ [km s^{-1}]	R_{peak} [kpc]	$V_c(R_{peak})$ [km s^{-1}]	$V_{2.2}/V_{200}$	n_{SF} [cm^{-3}]	T_{SF} [10^3 K]	ϵ_{SF}
G.321	239.8	5.69	243.8	1.90	1.0	9	0.65
G.322	233.6	5.69	237.5	1.85	1.0	9	0.65
G.323	233.3	5.69	237.8	1.93	1.0	9	0.65
ERIS	206.0	1.34	238.0	1.66	5.0	30	0.10
MollitorB	233.0	9.63	233.0	—	2.7	3	0.01
MW obs.	221±18	—	—	$1.11^{+0.22}_{-0.20}$	—	—	—
	Box [Mpc h^{-1}]	z_{ini}	Ω_0	Ω_{Λ}	Ω_b	H_0 [$\text{km s}^{-1} \text{ Mpc}^{-1}$]	σ_8
G.321	20	60	0.30	0.70	0.045	70	0.80
G.322	20	60	0.30	0.70	0.045	70	0.80
G.323	20	60	0.30	0.70	0.045	70	0.80
ERIS	90	90	0.24	0.76	0.042	73	0.76
MollitorB	20	50	0.276	0.724	0.045	70.3	—
MW obs.	—	—	—	—	—	—	—

Table 1 Parameters of GARROTXA321 (G.321), GARROTXA322 (G.322) and GARROTXA323 (G.323) simulations at $z=0$. r_{vir} is assumed to be equal to r_{97} . Hot, warm and cold gas is at $T > 3 \times 10^5 \text{ K}$, $3 \times 10^5 \text{ K} > T > 3 \times 10^4 \text{ K}$ and $T < 3 \times 10^4 \text{ K}$, respectively. Comparison with other state of the art simulations is also shown (ERIS simulation (Guedes et al. 2011) and model B in Mollitor et al. (2014)). All parameters are well defined in the text (Sec. 3.1). Observed values for the MW have been obtained from Ferrière (2001); Flynn et al. (2006); Du et al. (2006); Hammer et al. (2007); Xue et al. (2008); Jurić et al. (2008); Dutton et al. (2010) and Kafle et al. (2014)

3.2. Dark matter component

As we have mentioned in the last section all dark matter particles inside virial radius are particles of the first

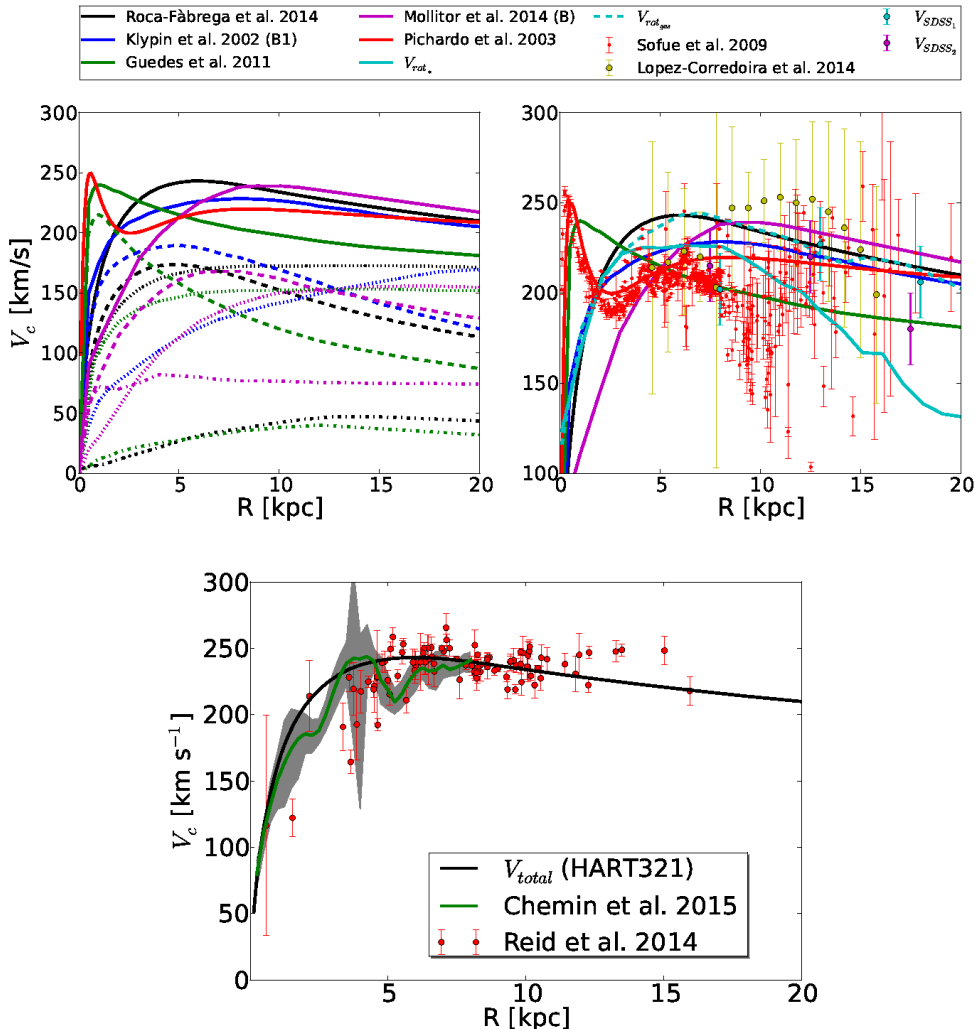


Figure 3. Top-left: Circular velocity curve of our simulated Milky Way sized galaxy model GARROTXA321 (black), Guedes et al. (2011) (green), model B1 in Klypin et al. (2002) (blue), Mollitor et al. (2014) (magenta) and analytical model in Pichardo et al. (2003) (red). The figure shows the contribution to the circular velocity $V_c = \sqrt{GM_{<r}/r}$, that is similar to the one we obtained from the true gravitational potential, of the various mass components: dark matter (short dashed curve), stars (long dashed), gas (dot-dashed) and total mass (solid curve). Top-right: Total circular velocity curves of the same models shown at left, observational data points and gas and stars rotation curves of our model GARROTXA321 (cyan dashed and solid lines, respectively). Data points come from two realizations of the rotation curve of the Milky Way from observations of blue horizontal-branch halo stars in the SDSS (Xue et al. 2008), in cyan and magenta dots, from López-Corredoira (2014), in green, and from Sofue et al. (2009), in red. Bottom: Observational circular velocity curve obtained using massive young star forming regions of the MW (Reid et al. 2014). The total V_c of our model GARROTXA321 at $z=0$ is shown as a black solid line. In Green we show the hypothetical gaseous rotation curve of the Milky Way obtained by Chemin et al. (2015) and in grey the 1σ range.

DM specie, the less massive one. In Fig. 4 we show the dark matter density profile as a function of radius (red circles) and the best fit of NFW profile for the model GARROTXA321 (upper yellow solid line). We avoid the central region ($R < 5$ kpc) in the fit of the NFW profile to avoid perturbations derived from the presence of baryons (adiabatic contraction). The best NFW fit gives a large value for the halo concentration that is $c = r_{vir}/r_s = 28.5$, 26.8 and 26.9 for GARROTXA321, GARROTXA322 and GARROTXA323, respectively. These values fall inside the observational range presented in Kafle et al. (2014) that is $21.1^{+14.8}_{-8.3}$. No core is observed in the central region of our models. The halo spin parameter as defined in Bullock et al. (2001) is $\lambda' = 0.019$, 0.017 and 0.022. These λ' values also fall well inside the range obtained by Bullock et al. (2001) after analysing more than

500 simulated halos (see figure 1 in Bullock et al. (2001)).

3.3. Gas component

In our models GARROTXA321, GARROTXA322 and GARROTXA323 the total gas mass inside the virial radius is $M_{gas} = 2.7$, 1.73 and $1.96 \times 10^{10} M_\odot$. In our model GARROTXA321 about $9.34 \times 10^9 M_\odot$ of gas mass is in cold gas phase ($T < 3 \times 10^4$ K) while for models GARROTXA322 and GARROTXA323 it is 1.52 and $1.86 \times 10^9 M_\odot$. For model GARROTXA321 the value is comparable to the total mass of the molecular, atomic and warm ionized medium inferred for the MW that is $\sim 7.3 - 9.5 \times 10^9 M_\odot$ (Ferrière 2001). For the rest of models presented here the amount of cold gas is smaller. This cold gas mass reduction is a consequence of an increase on the star formation at early ages, that in its turn is

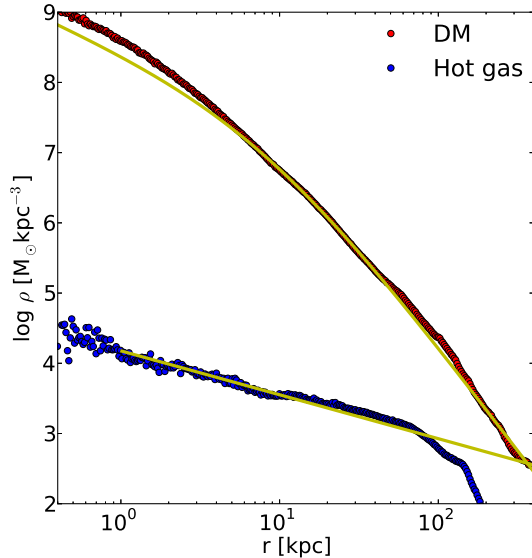


Figure 4. Average dark matter (red dots) and hot gas ($T > 3 \times 10^5$ K, blue dots) density profiles at $z=0$. The upper solid yellow line show the best NFW profile fit to the dark matter mass distribution, in the range from 5 kpc, outside bar-bulge region, to r_{vir} . The lower solid yellow line show the best fit power-law profile to the hot gas mass distribution between 5 and 20 kpc. The DM best fit NFW profile is characterized by a large halo concentration parameter $c=28.5$ as the dark matter halo contracts in response to the condensation of baryons in its center (adiabatic contraction). In the inner region it can be clearly observed that no DM core is present. The hot gas best fit power-law profile gives a slope of $\rho_X = -0.62$.

provoked by the higher aggressivity in the refinement criteria. This increase on the star formation is the only effect we have observed when changing the refinement criteria and it is consequence of resolving a larger number of small dense regions in where the SF criteria is accomplished.

At $z=0$, the SF criteria is satisfied only in the inner disk regions ($R < 7$ kpc). This spatially limited star formation accords with the young stellar distribution shown in Fig. 1 and also with the decrease of the Star Formation Rate (SFR) at $z=0$ that can be seen in Fig. 10.

The hot gas mass ($T > 3 \times 10^5$ K) is around 1.22, 0.98 and $1.32 \times 10^{10} M_\odot$ for models GARROTXA321, GARROTXA322 and GARROTXA323, respectively, and this is the fraction that has opacity in the X-ray region, and then, it is comparable with observations of ionized oxygen (Gupta et al. 2012). In Fig. 5 we show the gas distribution as function of temperature in model GARROTXA321. Each panel show the distribution of gas at different temperatures (see figure caption). As can be seen in this figure, and also in Fig.1, cold gas is placed in disk region while hotter gas is embedded within the dark matter halo. Contrary to the standard assumption hot gas do not follow the dark matter radial distribution. This can be seen in Fig. 4 where we show the dark matter density distribution (red) and the hot gas density distribution (blue). The hot gas density distribution inside $r=100$ kpc can be fitted by a power law ($\rho_{hotgas}(r) \propto r^{-\alpha}$). After fitting data from models GARROTXA321, GARROTXA322 and GARROTXA323 we have obtained that hot gas density distribution scale fac-

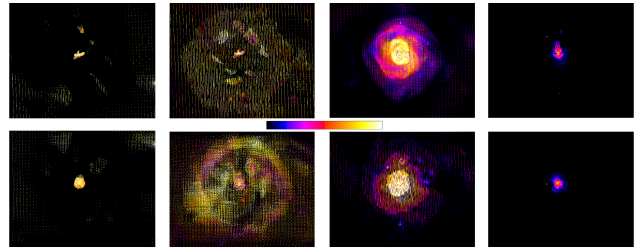


Figure 5. Edge on (top) and face on (bottom) views of gas density at $z=0$ in model GARROTXA321, as function of its temperature. From left to the right, 10^3-10^5 K, $10^5-3 \times 10^5$ K, $3 \times 10^5-10^6$ K, 10^6-10^7 K. All panels span 508 kpc in the vertical direction and 640 kpc in the horizontal. In colour we show the gas temperature from the minimum value in the range (black) to the maximum (white). Note that temperature ranges have changed when compared with the ones in Fig.1. Here we have used new ranges to split the hot gas component according to the definition we use in this work ($T > 3 \times 10^5$ K), that is X-ray luminous gas.

tors (α) of these models are -0.62, -0.83 and -0.67, respectively. These results, although they are close to, they are slightly higher than values used to fit analytical models of hot gas in dark matter halos (-0.9 in Anderson & Bregman 2010) and the ones obtained in other similar models like ERIS (-1.1 in Guedes et al. 2011). The hot gas density distribution power law fit for model GARROTXA321 is shown in Fig. 4 as the bottom yellow straight line.

In Sec. 4 we present our results of the study of hot gas distribution and also comparisons between our model and the observational values.

3.4. Stellar component

The total stellar mass in the virial radius of our models is $M_* = 6.1-6.2 \times 10^{10} M_\odot$, that is comparable with values estimated for the Milky Way ($4.5 \times 10^{10} - 7.2 M_\odot$ in Flynn et al. (2006) and Licquia & Newman (2014)). However, if we observe the relation between stellar mass and total mass (see Fig. 6) derived from our models (blue dots) and also from observations of the MW (shadowed region) we see that most of them fall quite above the M_*/M_{vir} predicted by cosmological theories. The same result is observed when using data from other recent MW-like simulations like ERIS simulation (Guedes et al. 2011) or the ones of Mollitor et al. (2014). This is itself an important result as we observe how theoretical models for the Λ CDM cosmology are not in agreement with observations and simulations. This result can be a consequence of that Λ CDM paradigm is wrong or that the galactic stellar mass in both, simulations and observations, is underestimated. In this work we have not studied this deeply, we deserve it for the future.

3.4.1. Stellar disk and stellar spheroid

Simulated galactic systems in our main models have both stellar disks and stellar spheroidal components (halo and/or bulge). To study properties of stellar galactic disks we need to distinguish first which stars belong to each component. To undertake this process we have used an extension of the kinematic decomposition proposed by Scannapieco et al. (2009). In Scannapieco et al. (2009) the authors used the ratio between the real stellar particle angular momentum perpendicular to the disk plane (j_z) and the one obtained assuming stellar particles follow a circular orbit

(computed from the circular velocity curve, j_c). Using this ratio it is easy to distinguish particles that are rotationally supported ($j_z=j_c$ for disk stars) from ones that are not ($j_z < j_c$ for spheroid stars). Here we decided to make additional cuts to improve this technique. We have done complementary cuts in metallicity, in the vertical coordinate $|z|$, in the angle between the rotation axis of each particle and the vector perpendicular to the plane ($\cos(\alpha)$) and in the distance to the galactic center (R). To avoid kinematic biases we have made first cuts that do not involve kinematics. We have started with the metallicity cut and next we have made a cut in the vertical coordinate, in radius, in $\cos(\alpha)$ and finally in j_z/j_c . It is evident that some of the restrictions we have imposed require from a previous knowledge of the disk plane position. To find this position we have used an iterative geometrical approach (pages 9 to 11 in Atanasijevic 1971). In this approach the plane that minimizes the total distance of all particles to it is selected. In the first iteration we have used only stars that are inside a sphere of 20 kpc centered to the center of mass of the first specie of DM particles that is the lightest one. After this first iteration we have only used stars that fall nearby the newly defined plane (i.e. $|z_{new}| < 5$ kpc). We have checked that after few iterations we get a plane that coincides with the disk plane defined by young stars and cold gas (see left panels of Fig. 1, Fig. 2 and Fig. 5).

After analysing the stellar distribution of our models in both, Cartesian and phase spaces, we have found the conditions that better distinguish disk from spheroid particles. In our main models these conditions are: $j_z/j_c > 0.55$, $|z| < 3.5$ kpc, $[\text{Fe}/\text{H}] > -0.5$, $\cos(\alpha) > 0.7$ and $R < 25$ kpc. All particles that do not accomplish one or more of these restrictions are considered spheroid particles. The result of this selection can be seen in Fig.7 where we show the stellar mass fraction as a function of j_z/j_c for model GARROTXA321, the result is similar for the other models. In this figure we show how well we trace the two main stellar components of the model: one centered at $j_z/j_c=1$, i.e. rotationally supported, and another at $j_z/j_c=0$. The mass of the rotationally supported component (disk) is around $M_d = 1.82, 2.17, 2.21 \times 10^{10} M_\odot$ and the one of spheroidal component $M_{sph} = 4.29, 3.93, 3.96 \times 10^{10} M_\odot$ for models GARROTXA321, GARROTXA322 and GARROTXA323, respectively. Comparing these results with previous studies (Guedes et al. 2011) and with observations (Flynn et al. 2006; Bovy & Rix 2013) we find that the spheroidal component in our models is slightly more massive and the disk is slightly lightest than the ones expected for the MW. When changing the aggressivity of the refinement criteria we observe that the disk mass changes accordingly. Disk mass become more massive when the aggressivity is higher. This relation is a consequence of that an increase on the refinement aggressivity drives to an increase on the number of stellar particles that are formed in dense gas regions inside the disk. Observing results from models presented here one can be concerned about if the massive spheroidal component is a large stellar concentration in the central region, a problem that was common in old cosmological simulations. However, as can be seen in the rotation

curves shown in Fig. 3, this is not the case here (the curves do not present a central peak). We have analyzed this spheroidal component and we have detected that it is a dense inner halo, not a massive bulge, combined with a triaxial structure that was formed in the mayor merger occurred at $z=3$ (see Sec. 3.1.1). We argue that the presence of such structures will not have a strong impact in our analysis of disk kinematical and dynamical properties. We claim this because the rotation curve, disk scale length and amount of gas, among others, remain realistic.

3.4.2. Disk properties

With the stellar disk/spheroid selection process we have found disk components that are a sample of 2.0, 6.0 and 18.7×10^5 particles for each one of our main models. We have also computed the mean volume and surface density of the disk, as function of radius. We have found that a single or a double exponential power law can be fitted to the data depending on the age of the selected population. In Fig. 8 we show the total disk surface density (black) as function of radius of the model GARROTXA321 at $z=0$. To the surface density curve we have fitted two exponential power laws (red and blue). We have obtained that $R_d=4.89$ kpc in the inner regions (2–6 kpc) and $R_d=2.21$ kpc in the outer ones (6–12 kpc). If we fit a single exponential to the whole radial range from 2 to 12 kpc we obtain that $R_d=2.56$ kpc, result that is in agreement with values obtained for the MW (e.g. 2.3 ± 0.6 kpc in Hammer et al. (2007) or 2.15 ± 0.14 kpc in Bovy & Rix (2013) using G-type dwarfs from SEGUE). It is important to note that, as can be seen in Fig. 8, a small concentration of stars is present in the central regions ($R < 2$ kpc). This concentration is caused by the presence of a young bar. In Fig. 9 we show the volumic density as function of the distance to the plane (z) of three disk populations split by age. We have selected a young (0–0.5 Gyr), intermediate (0.5–4.0 Gyr) and old (4.0–11.0 Gyr) disk populations. The density have been computed using vertical bins of $\Delta z=0.2$ kpc and only stars that are in between $R=2$ and $R=9$ kpc. We have found that the scale height (h_z) of each population when fitting a decreasing exponential to the vertical density distribution in the range $0.1 \text{ kpc} < |z| < 2.0 \text{ kpc}$, is $h_z=277$ pc for the young, $h_z=959$ pc for the intermediate and $h_z=1356$ pc for the old populations (these values are for GARROTXA321 simulation, values for the other models can be found in Tab. 1. Scale height values are compatible with the ones expected for the MW. Observations show that the vertical distribution of stars in the MW can be fitted by two exponential with a scale heights of $h_z=300 \pm 60$ pc (Jurić et al. 2008) and $h_z=600-1100 \pm 60$ pc (Du et al. 2006). Our values also follow the relation proposed by Yoachim & Dalcanton (2006) that argue that disk scale height in edge on galaxies increases in disks following $z_0 \approx 2h_z=610(V_c/100) \text{ km s}^{-1}$.

3.4.3. Star formation history (SFH)

In our simulations stars are being formed with a $\text{SFR}_{z=0}=0.27 M_\odot \text{ yr}^{-1}$, $0.18 M_\odot \text{ yr}^{-1}$ and $0.41 M_\odot \text{ yr}^{-1}$, for models GARROTXA321, GARROTXA322 and

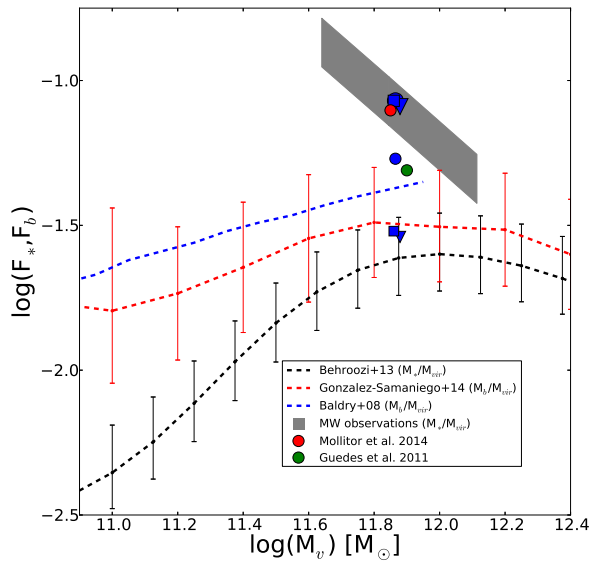


Figure 6. Comparison between $M_{*,b}/M_{vir}$ theoretical predictions and the ones obtained from observations and simulations. Blue items show M_{*}/M_{vir} values in our models GARROTXA321 (circles), GARROTXA322 (triangles) and GARROTXA323 (squares), using total stellar mass (large items) and only disk stellar mass (small items), see Sec. 3.4.1 for information about stellar disk selection process. Observed range for the M_{*}/M_{vir} in the Milky Way Galaxy (Flynn et al. 2006; Xue et al. 2008; Licquia & Newman 2014; Gibbons et al. 2014) is shown as a grey shadowed region. Red dot show the M_{*}/M_{vir} value obtained in model B presented by Mollitor et al. (2014). Green dot shows M_{*}/M_{vir} of the ERIS simulation (Guedes et al. 2011). Behroozi et al. (2013) observational M_{*}/M_{vir} curve inferred from observations at $z=0.1$, with no distinction between blue or red galaxies, and its errors, is shown as dashed black line. As a red dashed line, results obtained for the M_b/M_{vir} relation in González-Samaniego et al. (2014) when using a semi-empirical model. The blue dashed line corresponds to the M_b/M_{vir} relation calculated by Baldry et al. (2008). As can be seen it becomes a challenge for Λ CDM to fit its theoretical predictions with observations.

GARROTXA323, respectively. These are values smaller than the one inferred by Robitaille & Whitney (2010) using Spitzer data, for the MW, that is $SFR=0.68-1.45 M_{\odot} \text{ yr}^{-1}$. In Fig. 10, top panel, we show the SFR as function of the redshift for the total (black), spheroidal (red) and disk (blue) components. We have computed the SFH using stars inside r_{vir} at $z=0$. In this figure it is easy to see that at slightly higher redshifts than $z=0$ the SFR values are in agreement with observations for the MW at $z=0$. As a shadowed region we show the predicted SFH for MW like halos derived from semi-analytical models that combine stellar mass functions with merger histories of halos (Behroozi et al. 2013). The peak in the SFH of our models occurs at slightly early ages than the one predicted for a MW-like galaxy. In the bottom panel we plot the total stellar mass as function of redshift. Some important results that can be appreciated from this figure are, first, that the spheroidal component is being build at high redshifts while disk starts its formation at around $z=2.5$ (~ 11 Gyr from the present time), just after the last major merger that was at $z=3$. Second, it is also important to note that the star formation of spheroidal component decrease quickly after $z\sim 2.4$ and become negligible at

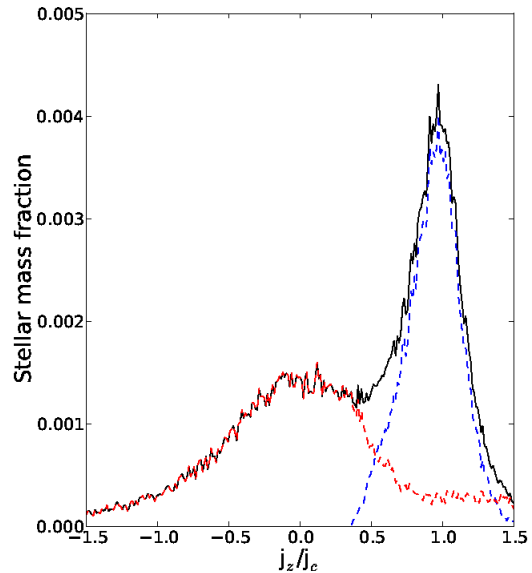


Figure 7. Stellar mass fraction as function of the orbital circularity parameter j_z/j_c , describing the degree of rotational support of a given stellar particle (black: all particles; red: spheroid; blue: disk). The stars in a centrifugally supported thin disk manifests itself in a sharply peaked distribution about unity. We have used all stellar particles inside disk region ($|z| < 0.5$ kpc and $r < 15$ kpc) of model GARROTXA321 at redshift 0.

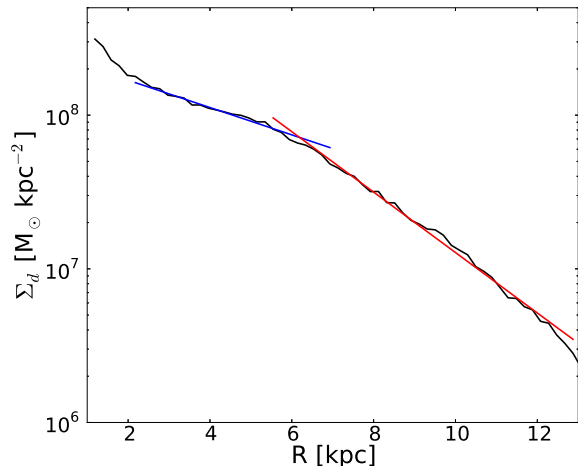


Figure 8. Stellar disk surface density profile as function of cylindrical radius R (black solid line). The solid blue and red lines show the best-fit exponential profiles to the inner and outer disk components, respectively. The inner component (2–6 kpc) has an $R_d=4.89$ kpc and the outer (6–12 kpc) an $R_d = 2.21$ kpc. If we fit the whole disk density profile from 2 to 12 kpc we obtain an $R_d = 2.56$ kpc. All results have been obtained analysing model GARROTXA321 at redshift 0.

around $z=0.5$. The disk SFR also decreases fast in the last time instants except for some short periods of star formation that can be a consequence of the accretion of small gaseous satellites. This reduction in the star formation when reaching $z=0$ is a consequence of the reduction of cold gas available for star formation. Several processes can lead to a reduction of the cold gas mass fraction. First, cold gas can be drastically consumed at higher redshifts due to a non-realistic implementation of physical parameters that controls star formation.

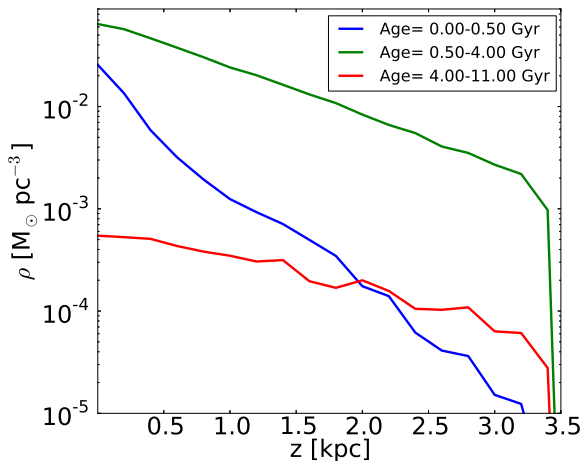


Figure 9. Vertical density profile of young (blue), intermediate (green) and old (red) disk stars in the model GARROTXA321 at redshift 0.

When such problem exists a large amount of old stars are present at $z=0$ in the inner disk region. In our models, as can be seen in Fig. 7, an old spheroid is present in the disk region, however this old stellar population is not big enough to account for the reduction of the observed cold gas component. Second, if stellar and SNe feedback is too efficient, an important amount of cold gas can be heated up and then to become unavailable for star formation. In this scenario what we would expect is that the fraction of hot gas increase with time, a behaviour that is not observed in our models. Finally a decrease in the cold gas inflow due to inhomogeneities in the circumgalactic medium (CGM) can also be a cause of the reduction of the SFR. If this last hypothesis is true we would observe only a small amount of cold gas present around our system, or falling from filaments, in the last Gyr. We argue that in our models the reduction of the cold gas component is a consequence of a combined effect of the first and the last hypothesis, however we deserve a deeper study for the future.

It is important to mention here that in this work we have used a code in where only a first approach of the metallic enrichment by SNe is implemented. In this approach three chemical species are used, i.e. alpha elements, iron elements and primordial gas (H). The information that can be obtained from this simplified chemical model will be discussed in a forthcoming paper.

4. MISSING BARYONS PROBLEM AND THE EXTRAPLANAR GAS

4.1. *The missing baryons problem*

The lack of baryonic mass in galaxies was confirmed when WMAP and Planck high precision data of the cosmic microwave background became available. This data revealed that the cosmic ratio between baryonic and total matter (Ω_b/Ω_M) is 3–10 times larger than the one observed in galaxies. For instance, Hoekstra et al. (2005) found a baryonic fraction for isolated spiral galaxies of 0.056 and for elliptical of 0.023 while Dunkley et al. (2009) presented a cosmic baryonic fraction from WMAP 5-year data of about 0.171 ± 0.009 . Some studies tried to solve this missing baryon problem

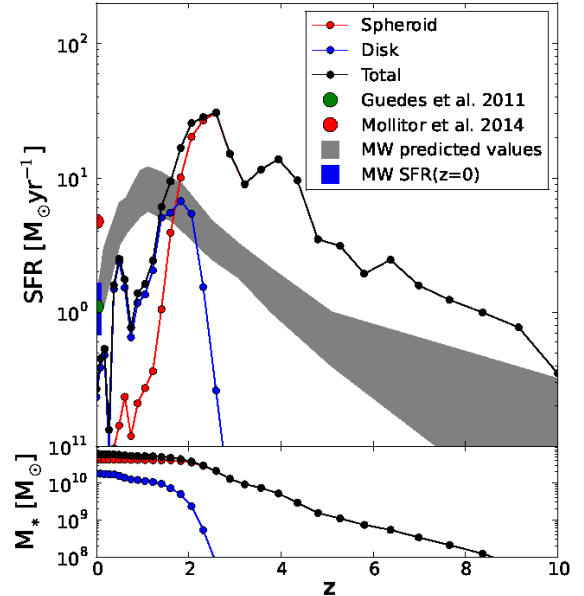


Figure 10. Star formation history (SFH), top, and total mass history, bottom, of all star particles identified within virial radius at $z=0$ in model GARROTXA321. Black, blue and red filled dots show the total, disk and spheroid star formation rates (top panel) and stellar mass (bottom panel), respectively, as a function of redshift. Grey shadowed region indicates the predicted SFH for a MW-like halo with $M_{97}=10^{12} M_{\odot}$ (Behroozi et al. 2013). Green and red big dots show total SFR at $z=0$ of models presented by Guedes et al. 2011 and Mollitor et al 2014 (B), respectively. The blue filled region shows the $z=0$ MW SFR range derived from observations by Robitaille & Whitney (2010).

proposing that galactic winds, SNe feedback or strong AGN winds ejected baryons to the circumgalactic medium (CGM). Others proposed that most of the gas never collapsed into the dark matter halos as it was previously heated by SNe of Population III, this is known as the preheating scenario. Thus, it has become clear that studying the CGM is necessary not only for finding the missing baryons, but also to understand its properties in the context of galaxy formation and evolution models. To further constrain galaxy evolution and find out which one of the proposed theories solves the missing baryon problem it is needed to measure the amount of warm-hot gas phase present in the CGM and also its metallicity. Results of such measures give information about the heating mechanism: hot gas with low metallicities is indicative of a Pop III SNe preheating while a more metallic gas suggest that it has been enriched in the disk via SNe and stellar winds. Supporting the first hypothesis, different authors agreed with the idea of very strong feedback driving galactic-scale winds, causing metal-enriched hot gas to be expelled out of the star-forming disk possibly to distances comparable to or beyond the virial radius. This process also lies in the heart of obtaining realistic simulations of disk galaxies (Guedes et al. 2011; Marinacci et al. 2014). By this mechanism gas is temporally placed far from star forming regions delaying the star formation and preventing the formation of an old bulge in the center of the system. From the analysis of OVII and OVIII X-Ray absorption lines in extragalactic lines of sight, several authors

obtained values for the hot gas distribution in the MW halo (Gupta et al. 2012, 2014) that suggest an important part of missing baryons are in this hot gas phase. They show that the warm-hot phase of the CGM is extended over a large region around the MW, with a radius over 100 kpc, with a mass around $10^{10} M_{\odot}$. Also from these observations some authors suggest that this component is in a non isotropic distribution, however, these measures are limited to directions with extragalactic sources (QSO, AGN) and as a consequence results are not conclusive. Other studies also suggest that the presence of this hot gas phase can explain part of the isotropic gamma-ray background observed in Fermi Gamma-ray Space Telescope (Feldmann et al. 2013).

4.2. Hot gas component in GARROTXA321

4.2.1. Spatial distribution

The amount of hot gas in our models is in between $M_{hot} = 0.98-1.32 \times 10^{10} M_{\odot}$. This hot gas that has a temperature above 3.0×10^5 K (has opacity in the X-rays) is embedded in the dark matter halo but mostly outside the stellar disk. We have computed hot gas values of the Hydrogen equivalent column density and emission measure (EM)¹ as:

$$N_H = \int_{los} n_H dl \quad (1)$$

$$EM = \int_{los} n_e^2 dl \quad (2)$$

where n_H is the hydrogen particles density, dl is an element of the path in the line of sight and n_e is the electron density.

In Fig.13 we show a full sky view of hot gas column density distribution in our model GARROTXA321. This figure has been obtained computing the column density of the hot gas from a position that is at 8 kpc from the galactic center, inside the simulated galactic disk, resembling the Sun position, and at an arbitrary azimuthal angle. We have obtained values that fall near the observational ranges, if a solar metallicity is assumed (see Tab. 3 and Gupta et al. 2012). On the other hand, when assuming lower metallicities, observations predict values that are above the ones find in our simulations. This change can give us information about the absorption of the local warm-hot intergalactic medium (WIMP). From this figure we also note that the distribution of hot gas inferred from all measures is far from isotropic. It is important to mention that in our models (see Fig. 1 and 13) we are do not detect a hot has thick disk component. This is important as it is under discussion what is the contribution of the hot gas thick disk to the observed X-ray emission/absorption. Another interesting result is that the gas distribution is not symmetric with respect to the disk plane what

suggest some degree of interaction with the extragalactic medium. To study this gas component and its interaction with the extragalactic medium we have analyzed the metallicity and velocities of hot gas cells. In Fig. 14 we show the metallicity distribution of the hot gas as seen from the Galactic center. We see that gas metallicity distribution does not depend on the azimuthal angle (θ) (Fig. 14, top panel) while it is clear that it depends on the vertical (ϕ) (Fig. 14, bottom panel). It is also clear that exists a low metallicity component at the northern hemisphere that is not present at the south where metallicity is much higher. It is important to note that in Fig. 14, bottom panel, we can distinguish a clear break in the hot gas distribution at low latitudes. This hole coincides with the position of the stellar/cold gas disk.

To put some light on the origin of this bimodality in the metals distribution we have made a set of three colour maps that show the projected metallicity and velocities at each one of the principal planes (see Fig. 15 and Fig. 16). Fig. 15 (X-Y plane, i.e. disk plane) shows that in general hot gas in the disk plane rotates following the disk rotation direction. Fig. 16 (X-Z plane, top and Y-Z, bottom) show a more complex scenario with several vertical motions and metallicity gradients. In this last figure it becomes clear that low and high metallicity hot gas vertical flows are present in the halo. It is also easy to detect that exists a bimodality in metallicity in the vertical direction and also that low-metallic hot gas flow has a mean motion that brings it from outside to inside the system, i.e. it is falling from the IGM. High-metallic hot gas flows observed in the southern hemisphere have a slower and more irregular motion than ones in the northern but, in general, they also move from inside to outside the system. While it is easy to understand and interpret why low-metallic hot gas is falling inside the system, and why in some cases hot metallic gas departs from the stellar disk region (SN feedback, stellar winds...), it is not so obvious why some clouds of such hot metallic gas, with sizes of tens of kpc, behaves differently. We suspect that this last high-metallic component could be associated with a small gaseous satellite that is passing through the system at $z=0$ (see Fig.17). To confirm all these hypothesis we have made the same velocity-metallicity maps as the ones in Fig. 15 and Fig. 16 for several snapshots back to $z = 0.5$. From the analysis of these snapshots we have confirmed that in some instants hot gas with enhanced metallicity depart from the disk due to feedback of stellar component. We have also seen that low metal flows appear coming from the CGM. Finally, at around $z=0$, we have seen that a gaseous satellite approaches to the main galaxy perturbing hot gas flows. The perturbation of the hot gas distribution by accretion of small satellites is an interesting process and it will deserve a more detailed study. Finally we have also compared the disk plane gas mean metallicity with that one of the hot gas in the halo and we have found that both components have similar mean metallicities that is around -0.64 dex (except for the high and low metallicity flows discussed here).

A conclusion we obtain from this metallicity and mean velocities preliminary study is that there exist hot gas flows from the IGM, both from low enriched medium and high enriched satellites. We also conclude that

¹ In this work we are not showing the dispersion measure values (DM) as they only differ by a factor of two from the N_H ones. N_H values are presented in Fig. 13. Although not presented here, DM values in our models are of the same order as the ones in Guedes et al. (2011).

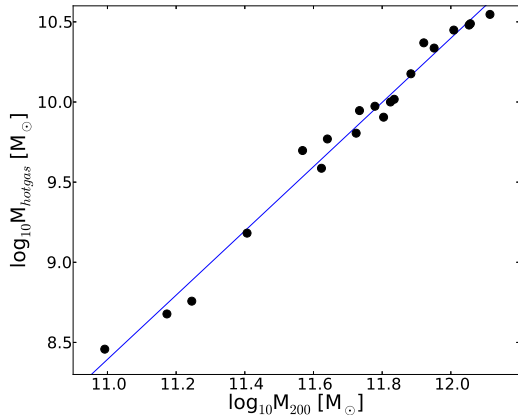


Figure 11. Total hot gas mass inside $r_{vir} = r_{200}$ as function of total virial mass. Corresponding models and their properties are presented in Tab. 2.

the disk has a smaller concentration of hot gas as a consequence of that SNe explosions and stellar winds bring it up to the halo. These results are coherent with what was proposed by Dekel & Birnboim (2006). In this work the authors proposed that for halos with $M_{vir} < 10^{12} M_{\odot}$ the accretion of cold gas by the cold flow dominates and it can avoid the formation of X-ray halo corona. In this case cold flow leads to the formation of star forming blue disk galaxies. On the other hand for systems with $M_{vir} > 10^{12} M_{\odot}$ they found that it dominates the gas shock-heating. In this last scenario red spheroidal galaxies with hot halo coronas and no star formation are produced as cold gas flows disappear. For masses near to $10^{12} M_{\odot}$ both processes are acting what is in agreement with results obtained here.

Finally in Tab. 2 and Fig. 11 we present results of the study of a possible correlation between the virial mass and the total hot gas in galaxies. Analysing several models, both MW-like models and other systems with higher and smaller masses, we have found that in general the higher the M_{vir} , the higher the total hot gas mass. A similar result was presented in Crain et al. (2010). In their work they analyzed a correlation that exist between X-ray luminosity and virial mass. They found that exist two linear correlations, one for $M_{vir} < 5 \times 10^{12}$ and another for $M_{vir} > 5 \times 10^{12}$. Our work is focused on MW-like galaxy systems i.e. low halo masses, and we have found a simple linear correlation (see Fig. 11), too. Although absolute values obtained in our work can not be directly compared with the ones of Crain et al. (2010) as we are using M_{hotgas} and they are using L_X , if finally confirmed this linear correlation will provide a new restriction to the virial mass in galaxies.

4.2.2. Total hot gas mass: accounting for the missing baryons

The baryonic fraction in our simulations, accounting only for the stellar and cold gas mass, falls in between 0.084 and 0.096. These numbers are far from the cosmic baryon fraction imposed value in our models that is $F_{b,U} = 0.15$. On the other hand, when comparing with observations we find that baryonic fraction in our simulations is close to observed values for isolated spiral

galaxies (0.056 in Hoekstra et al. 2005) and far from the observed cosmic value ($F_{b,U} = 0.171 \pm 0.009$ Dunkley et al. 2009). These results suggest that warm-hot gas embedded in the dark matter halo can account for part of the missing baryons. However it is clear that values for the baryonic fraction, also when adding this baryonic component (0.107–0.120), are still far from the cosmic values inferred from WMAP and Planck. We argue that these still missing baryons can be placed in the IGM, in the filaments and far from the main galactic systems (Rasheed et al. 2010). As pointed out in Sec. 4.2.1 the presence of this WHIM can lead to an overestimation of the hydrogen equivalent column density. Another process that can affect the total amount and the distribution of halo hot gas is the presence of an AGN in the central region of the galactic system. In our models we have not implemented the AGN feedback from the central black hole. Nevertheless, it is still open to debate how a relatively low mass black hole, as the one in the real MW, affects or not gas properties of galactic systems.

4.2.3. Total hot gas mass: are results from observations biased?

As previously mentioned it is difficult to infer the total hot gas mass in the MW by using the available data from observations. Matter in the CGM is hot ($T = 10^5 - 10^7$ K) and tenuous ($n \simeq 10^{-5} - 10^{-4} \text{ cm}^{-3}$). Plasma in these conditions couples with radiation mainly through electronic transitions of light elements (C, N, O) in their He-like and H-like ionization stages. The strongest of these transitions falling in the soft X-rays. Due to the extreme low densities and small optical length of the CGM, detection of the absorption/emission features produced by this material has proved particularly challenging with the still limited sensibility of the gratings on board Chandra and XMM-Newton. As a consequence, observations in only a few number of line of sight directions have proved useful to observe X-ray absorption in quasar spectra. In this scenario it is clear that simulations can play an important role in the study of hot gas as they let us to obtain its real distribution in simulated galactic systems. To have all this information allows us to study how observational techniques can lead to biased results for the total hot gas in the galactic system.

To undertake this work we have located our mock observer at 8 kpc from the galactic center (i.e. similar to solar position) in the galactic plane and at a random azimuthal angle, inside our MW-like simulations. For comparison we refer the reader to observations of OVII column densities presented in Gupta et al. (2012) and to total hot gas values they obtained. In Tab. 3 we show the results we have obtained when making observations to a similar number of randomly distributed directions into the sky as the ones in Gupta et al. (2012). As in our simulations we have not realistic chemical species like oxygen we have assumed that we are observing all hot gas, and present the column densities measured in each line of sight. As it is common in the literature (e.g. Gupta et al. 2012; Bregman & Lloyd-Davies 2007), we have assumed a spherical uniform gas distribution for the hot gas halo. As a first attempt, we have estimated, from the column density values at each direction, the total galactic hot gas mass, assuming a path length of

Model	Halo #	z	M_{200} [$10^{11} M_{\odot}$]	r_{200} [kpc]	M_{star} [$10^{11} M_{\odot}$]	M_{gas} [$10^{10} M_{\odot}$]	M_{hotgas} [$10^9 M_{\odot}$]	$M_{coldgas}$ [$10^9 M_{\odot}$]	ϵ_{SF}	DM_{sp}	n_{ref}
GARROTXA240	1	1.0	8.34	183.05	1.31	3.64	23.4	12.6	0.10	3	11
GARROTXA240	1	0.25	11.3	203.09	1.63	4.78	30.2	17.2	0.10	3	11
GARROTXA240	1	0.0	13.0	211.71	1.75	6.86	35.2	18.8	0.10	3	11
GARROTXA241	1	0.67	8.94	186.89	1.40	3.60	21.7	11.3	0.50	3	11
GARROTXA242	1	1.0	7.65	179.28	1.04	2.76	15.0	10.6	0.70	4	10
GARROTXA242	1	0.25	10.2	198.91	1.12	3.63	28.1	6.33	0.70	4	10
GARROTXA242	1	0.0	11.4	207.35	1.15	5.23	30.8	1.63	0.70	4	10
GARROTXA250	3	1.0	2.55	128.57	0.14	0.95	1.52	6.24	0.70	4	11
GARROTXA250	3	0.25	4.37	151.82	0.18	2.63	5.88	16.0	0.70	4	11
GARROTXA250	3	0.0	5.30	164.98	0.20	2.23	6.39	12.4	0.70	4	11
GARROTXA260	4	1.0	0.982	92.20	0.03	0.75	0.287	6.17	0.5	3	11
GARROTXA260	4	0.25	1.49	106.64	0.04	0.73	0.476	5.79	0.5	3	11
GARROTXA260	4	0.0	1.76	113.50	0.04	0.80	0.572	5.49	0.5	3	11
GARROTXA320	5	1.0	4.20	145.64	0.60	8.83	3.86	4.10	0.60	4	11
GARROTXA320	5	0.25	6.01	168.45	0.63	1.18	9.41	1.26	0.60	4	11
GARROTXA320	5	0.0	6.67	175.59	0.64	1.46	10.0	0.405	0.60	4	11
GARROTXA321	5	1.5	3.70	139.71	0.54	1.33	4.98	6.17	0.65	5	11
GARROTXA321	5	0.67	5.42	161.59	0.58	2.66	8.84	8.99	0.65	5	11
GARROTXA321	5	0.25	6.37	171.98	0.61	1.78	8.04	7.91	0.65	5	11
GARROTXA321	5	0.0	6.84	175.59	0.61	2.17	10.4	9.34	0.65	5	11

Table 2

M_{200} vs. hot gas mass inside R_{200} in our set of N-body plus hydrodynamics simulations. We also show the most relevant changes in the initial parameters, from the ones used in the model GARROTXA321 (see Tab. 1 for the definition of the parameters).

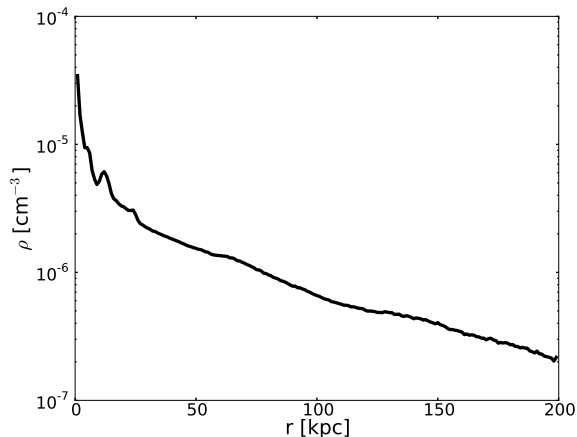


Figure 12. Spherically averaged hot gas density ($T > 3 \times 10^5$ K) as function of radius for the model GARROTXA321 at $z = 0$.

$L = 239$ kpc = r_{vir} . We have found that using the spherical uniform approach, the total hot gas mass is systematically overestimated (see Tab. 3 last column). This is a consequence of that the density distribution in our model is not uniform but it decreases as a power-law (see Fig. 4 and 12). However, this calculation is not very useful, as it requires an a-priori knowledge of the CGM path length (L) which is observationally unknown.

A popular technique among observational studies (i.e. Gupta et al. 2012; Bregman & Lloyd-Davies 2007) is to take advantage of the two observables for the hot gas in the CGM: the column density (N_H) and the emission measure (EM). This technique uses these two quantities to derive the total hot gas mass with no need of imposing an a-priori mean density or optical path length. We show results from using this technique in Tab. 4, both for the optical path length, the mean density and the total hot gas mass. In this case, as can be seen in the table, re-

	l [deg]	b [deg]	N_H [10^{19}cm^{-2}]	$M_{total, Hotgas}$ [$10^{10} M_{\odot}$]
FoV1	179.83	65.03	2.59	4.57
FoV2	17.73	-52.25	1.31	2.31
FoV3	91.49	47.95	2.96	5.21
FoV4	35.97	-29.86	2.81	4.96
FoV5	289.95	64.36	2.62	4.62
FoV6	92.14	-25.34	2.06	3.63
FoV7	287.46	22.95	2.62	4.62
FoV8	40.27	-34.94	2.59	4.57

Table 3

Mock observations of eight randomly distributed directions in the sky, in our GARROTXA321 simulation at $z = 0$. The total hot gas mass in the simulation, up to r_{vir} , is $M_{vir} = 1.2 \times 10^{10} M_{\odot}$.

We have defined hot gas as gas at $T > 3 \times 10^5$ K. We have assumed $L = 230.1$ kpc = r_{vir} .

sults show an underestimation of the total hot gas mass by factors $\sim 0.7-0.1$, result that is independent on the observed direction. Again this result is a consequence of that the real density distribution of our model is not uniform but decreasing with radius as a power law.

As a conclusion we state that using both, column density plus imposed optical depth (independently of using the value from a single observation or the mean) or a combination of column density and emission measure, we are not able to obtain the real hot halo gas mass, when assuming it is isotropically distributed in the galactic halo. Nevertheless, these measurements, particularly the observational method in the literature using both N_H and EM are useful to get a lower limit and an order of magnitude estimate of the total hot gas mass of the halo. The work is in progress to find the density profile that will allow us to get the best hot halo gas mass estimation, from observations.

5. CONCLUSIONS

In this paper we have introduced a new set of MW-like cosmological N-body plus hydrodynamics simulations. Their resolution and realism are high enough to allow us

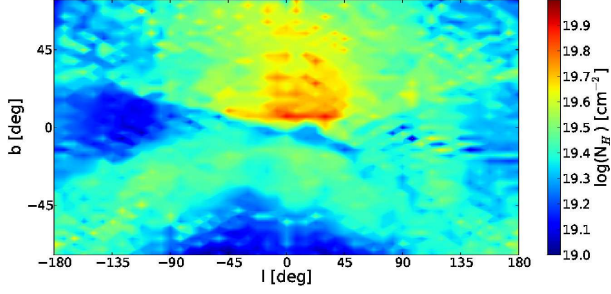


Figure 13. Hot gas ($T > 3 \times 10^5$ K) column density (top) in a full sky view of simulation GARROTXA321 in galactic coordinates, at $z = 0$. All values have been computed as observed from $R = 8$ kpc and at an arbitrary azimuthal angle.

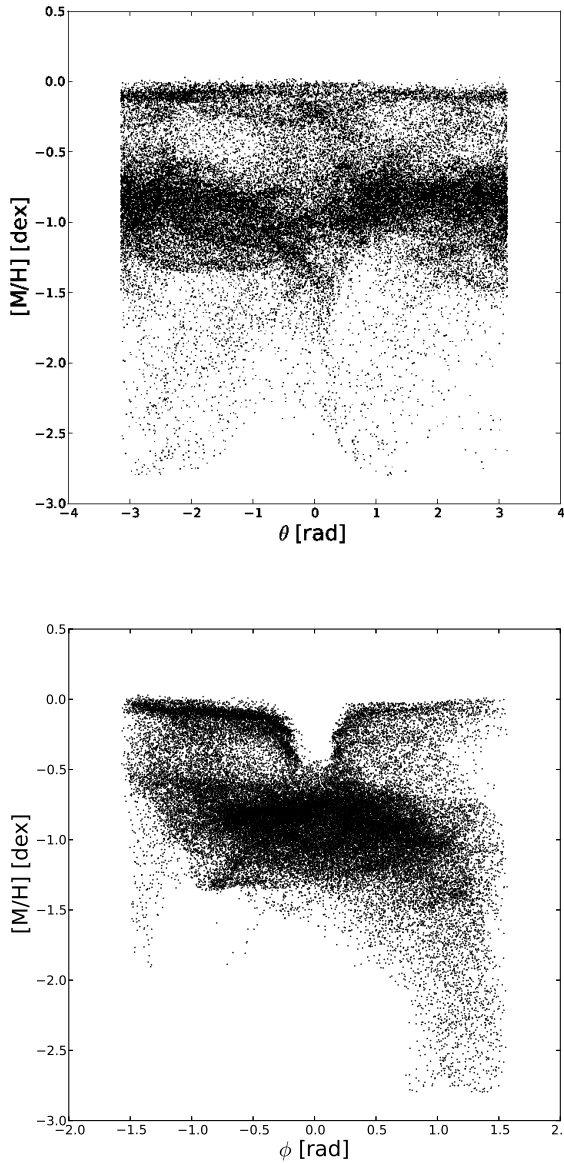


Figure 14. Hot gas ($T > 3 \times 10^5$ K) view in spherical galactic coordinates of the GARROTXA321 model, at $z = 0$. Top: metallicity as function of the azimuthal angle. Bottom: metallicity as function of the vertical angle. All values have been computed as observed from the galactic center.

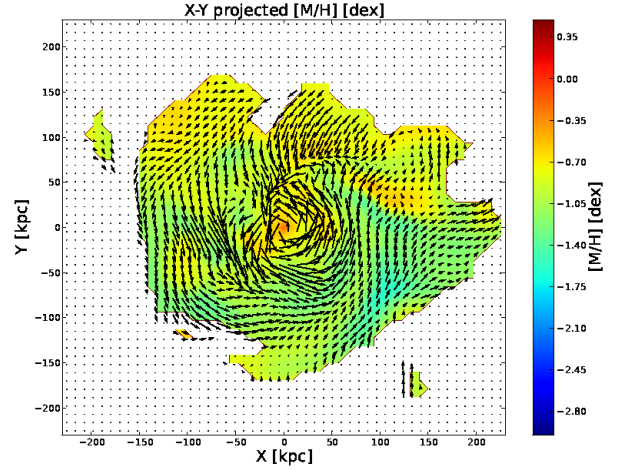


Figure 15. Hot gas ($T > 3 \times 10^5$ K) projected metallicity (colour map) and galactocentric velocity direction (arrows) in the principal plane X-Y of the GARROTXA321 model, at $z = 0$.

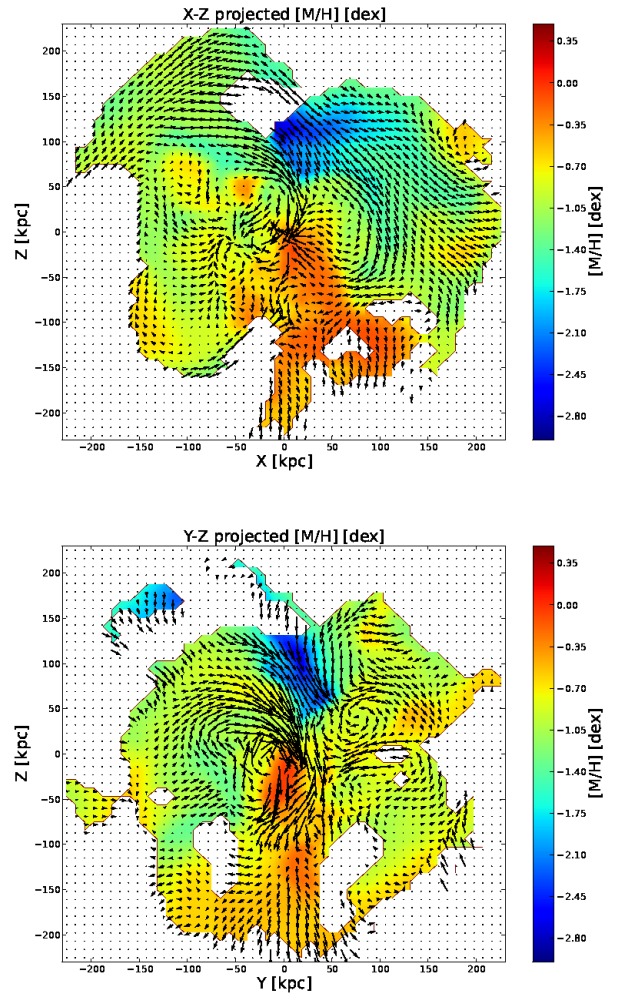


Figure 16. Hot gas ($T > 3 \times 10^5$ K) projected metallicity (colour map) and galactocentric velocity direction (arrows) in two principal planes, X-Z (top) and Y-Z (bottom) of the GARROTXA321 model, at $z = 0$.

	EM [$10^{-3}\text{cm}^{-6}\text{pc}$]	L [kpc]	n [10^{-4}cm^{-3}]	$M_{total,Hotgas}$ [$10^{10}M_{\odot}$]
FoV1	2.03	40.2	2.2	0.11
FoV2	0.16	111.3	0.4	0.40
FoV3	1.58	53.7	1.7	0.21
FoV4	0.79	56.6	1.2	0.17
FoV5	0.89	80.5	1.1	0.42
FoV6	1.40	59.1	1.5	0.25
FoV7	0.98	74.1	1.1	0.36
FoV8	0.61	116.5	0.7	0.88

Table 4

Emission Measure (EM) values from the same eight randomly distributed directions in the sky as in Tab. 3. Using EM and N_H values we have computed the path length (L) and hot gas volumic density (n). Finally we show the total hot gas mass obtained when assuming a sphere with constant density (n) and its radius equal to the path length (L). The real total hot gas mass in the simulation is $M_{vir} = 1.2 \times 10^{10} M_{\odot}$.

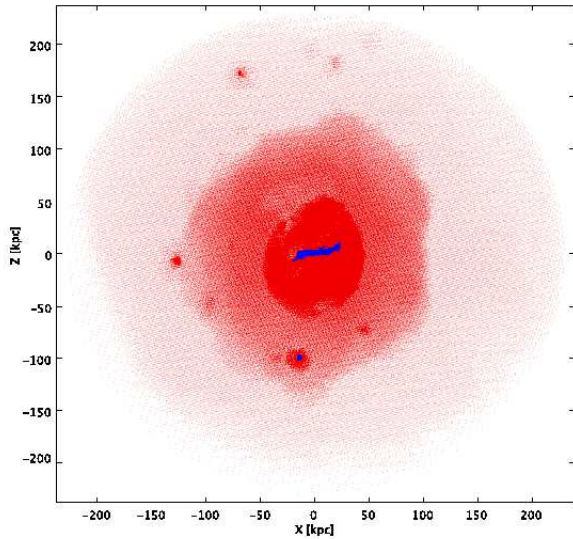


Figure 17. Warm-hot gas ($10^5 \text{ K} < T < 10^6 \text{ K}$) in red and cold gas ($T < 10^4 \text{ K}$) in blue, in the simulation GARROTXA321, at $z = 0$.

to study stellar kinematics (Roca-Fàbrega et al. 2013, 2014) and evolution of large scale structures of these kind of galaxies. Most stellar disk general parameters in our models are in agreement with observational ranges for the MW. Disk scale length and scale height, as well as their dependence on the stellar age, are well reproduced. Disk also shows a large variety of large scale structures like spirals, rings and bars and also a flared and warped configuration. The quality of our models is comparable to the most recent works presented by Guedes et al. (2011) and Mollitor et al. (2014). A detailed comparison can be seen in Tab. 1. Our models have similar or better number of stellar and gaseous particles/cells, spatial resolution and minimum mass per particle than the ones in such other works. In addition, as we have shown in Fig. 3, our circular velocity curves are in a very good agreement with recent observations. We have also analyzed the SFH in our simulations. We have found that our SFR values at $z=0$ fall within of the 2-sigma mean observational value. On the other

hand the SFH peak in our models occurs at higher redshift than the one predicted (Behroozi et al. 2013). In the most recent and realistic MW-like simulations (Guedes et al. 2011; Mollitor et al. 2014; Bird et al. 2013), the predicted SFH is also not well reproduced. We have also found that total gas mass and its distribution in temperature slightly differ from MW observations. This misfit in SFH is usual in simulations due to the lack of understanding of subgrid physics and to the difficulty of accounting for all physical processes involved in the formation and evolution of galaxies. Studies like ours will help to constrain such subgrid models. Recently, it has been proposed that to include a kinematic feedback can solve the early star formation issue and thus to change the position of the SFH peak. However, the use of this process is not a very realistic solution and it is still in discussion if it is useful or not.

The work presented here has been focused into study the distribution and the amount of potentially X-ray emitting gas ($T > 3 \times 10^5$) in our simulations. Our goal has been to compare properties of hot gas in our simulation with hot halo corona X-ray observations from the MW and external galaxies. To compare the hot gas distribution in our simulations with the one in observations we have made hot gas column density mock observations. Conclusions on this part follows:

- Hot gas is not distributed homogeneously all around the galactic halo.
- There is no evidence of a hot gas thick disk in our models.
- By using the real mass of warm-hot gas in our simulations we conclude that about 53%–80% of the missing baryons can be accounted by hot gas in the halo corona. The exact value depends on the simulated galactic system (e.g. halo mass). We argue that the lacking baryons could be placed in filaments (IGM), not inside main galactic systems, as preheated warm-hot gas (Rasheed et al. 2010). It is important to mention that in our simulations AGN feedback from a central galactic black hole has not been implemented. It is still open to debate how a relatively low mass black hole, as the one in the real MW, could affect the mass and temperature distribution of the hot halo gas and thus the SFH.
- Hot gas density follows several streams in the halo that can be detected because of their changes in kinematics and metallicity. We have seen how low metallicity streams come from the IGM while others with higher metallicity depart from the disk. We have also detected the infall of high metallicity gas that can be interpreted as coming from a satellite accretion.
- The total hot gas mass in the halo can not be recovered when assuming a spherical uniform gas distribution. In our model the real hot gas density distribution lead to an overestimation when using the mean column density plus a fixed optical depth under the spherical uniform assumption. On the

other hand it drives to an underestimation of the total hot gas mass when we use the column density plus the emission measure when using the same assumption.

- Following previous works we have found that a clear relation exist between total hot gas mass and virial mass of halos. This result is important as it becomes new method to constrain the total mass of galactic systems, such as the Milky Way.

Through this paper we have compared our results with other simulations in which different codes, analysis techniques, initial conditions, box width and also subgrid models were used. We have also analyzed several galactic systems that have different assembling histories, initial conditions and environment, and we have also made analysis at different redshifts. Results from all such different scenarios mostly coincide. This coinciding results lets us to state that although a deeper analysis may be needed, conclusions presented here do not depend of such parameters.

ACKNOWLEDGMENTS

We thank A. Klypin and A. Kravtsov for providing us the numerical codes. We thank HPC project, T. Quinn and N. Katz for the implementation of TIPSYP package. This work was supported by the MINECO (Spanish Ministry of Economy) - FEDER through grant AYA2012-39551-C02-01 and ESP2013-48318-C2-1-R. The simulations were performed at the Supercomputer Miztli of the DGTIC-UNAM, and at Atocatl and Abassi2, HPC facility of the Institute of Astronomy-UNAM.

REFERENCES

- Abadi M. G., Navarro J. F., Steinmetz M., Eke V. R., 2003, *ApJ*, 591, 499
- Agertz O., Teyssier R., Moore B., 2011, *MNRAS*, 410, 1391
- Anderson M. E., Bregman J. N., 2010, *ApJ*, 714, 320
- Atanasijevic I., ed. 1971, *Selected exercises in galactic astronomy* Vol. 26 of *Astrophysics and Space Science Library*
- Baldry I. K., Glazebrook K., Driver S. P., 2008, *MNRAS*, 388, 945
- Behroozi P. S., Wechsler R. H., Conroy C., 2013, *ApJ*, 770, 57
- Bird J. C., Kazantzidis S., Weinberg D. H., Guedes J., Callegari S., Mayer L., Madau P., 2013, *ApJ*, 773, 43
- Bogdán Á., Gilfanov M., 2011, *MNRAS*, 418, 1901
- Bovy J., Rix H.-W., 2013, *ApJ*, 779, 115
- Boylan-Kolchin M., Bullock J. S., Sohn S. T., Besla G., van der Marel R. P., 2013, *ApJ*, 768, 140
- Bregman J. N., Lloyd-Davies E. J., 2007, *ApJ*, 669, 990
- Brook C. B., Stinson G., Gibson B. K., Roškar R., Wadsley J., Quinn T., 2012, *MNRAS*, 419, 771
- Brooks A. M., Solomon A. R., Governato F., McCleary J., MacArthur L. A., Brook C. B. A., Jonsson P., Quinn T. R., Wadsley J., 2011, *ApJ*, 728, 51
- Bryan G. L., Norman M. L., 1998, *ApJ*, 495, 80
- Bullock J. S., Dekel A., Kolatt T. S., Kravtsov A. V., Klypin A. A., Porciani C., Primack J. R., 2001, *ApJ*, 555, 240
- Ceverino D., Dekel A., Bournaud F., 2010, *MNRAS*, 404, 2151
- Ceverino D., Klypin A., 2009, *ApJ*, 695, 292
- Chemin L., Renaud F., Soubiran C., 2015, *ArXiv e-prints*
- Colín P., Avila-Reese V., Vázquez-Semadeni E., Valenzuela O., Ceverino D., 2010, *ApJ*, 713, 535
- Crain R. A., McCarthy I. G., Frenk C. S., Theuns T., Schaye J., 2010, *MNRAS*, 407, 1403
- Crain R. A., McCarthy I. G., Schaye J., Theuns T., Frenk C. S., 2013, *MNRAS*, 432, 3005
- Cuesta A. J., Prada F., Klypin A., Moles M., 2008, *MNRAS*, 389, 385
- Dekel A., Birnboim Y., 2006, *MNRAS*, 368, 2
- Dekel A., Birnboim Y., Engel G., Freundlich J., Goerdt T., Mumenthaler M., Neistein E., Pichon C., Teyssier R., Zinger E., 2009, *nat*, 457, 451
- Du C., Ma J., Wu Z., Zhou X., 2006, *MNRAS*, 372, 1304
- Dunkley J., Komatsu E., Nolte M. R., et al. 2009, *ApJS*, 180, 306
- Dutton A. A., Conroy C., van den Bosch F. C., Prada F., More S., 2010, *MNRAS*, 407, 2
- Duval M. F., Athanassoula E., 1983, *A&A*, 121, 297
- Fall S. M., Efstathiou G., 1980, *MNRAS*, 193, 189
- Feldmann R., Carollo C. M., Mayer L., 2011, *ApJ*, 736, 88
- Feldmann R., Hooper D., Gnedin N. Y., 2013, *ApJ*, 763, 21
- Ferland G. J., Korista K. T., Verner D. A., Ferguson J. W., Kingdon J. B., Verner E. M., 1998, *PASP*, 110, 761
- Ferrière K. M., 2001, *Reviews of Modern Physics*, 73, 1031
- Flynn C., Holmberg J., Portinari L., Fuchs B., Jahreiß H., 2006, *MNRAS*, 372, 1149
- Forman W., Jones C., Tucker W., 1985, *ApJ*, 293, 102
- Gibbons S. L. J., Belokurov V., Evans N. W., 2014, *MNRAS*, 445, 3788
- González-Samaniego A., Colín P., Avila-Reese V., Rodríguez-Puebla A., Valenzuela O., 2014, *ApJ*, 785, 58
- González-Samaniego A., Vázquez-Semadeni E., González R. F., Kim J., 2014, *MNRAS*, 440, 2357
- Governato F., Brook C., Mayer L., Brooks A., Rhee G., Wadsley J., Jonsson P., Willman B., Stinson G., Quinn T., Madau P., 2010, *nat*, 463, 203
- Governato F., Mayer L., Wadsley J., Gardner J. P., Willman B., Hayashi E., Quinn T., Stadel J., Lake G., 2004, *ApJ*, 607, 688
- Governato F., Willman B., Mayer L., Brooks A., Stinson G., Valenzuela O., Wadsley J., Quinn T., 2007, *MNRAS*, 374, 1479
- Guedes J., Callegari S., Madau P., Mayer L., 2011, *ApJ*, 742, 76
- Gupta A., Mathur S., Galeazzi M., Krongold Y., 2014, *APSS*
- Gupta A., Mathur S., Krongold Y., Nicastro F., Galeazzi M., 2012, *ApJ*, 756, L8
- Haardt F., Madau P., 1996, *ApJ*, 461, 20
- Hagihara T., Yao Y., Yamasaki N. Y., Mitsuda K., Wang Q. D., Takei Y., Yoshino T., McCammon D., 2010, *PASJ*, 62, 723
- Hammer F., Puech M., Chemin L., Flores H., Lehnert M. D., 2007, *ApJ*, 662, 322
- Hoekstra H., Hsieh B. C., Yee H. K. C., Lin H., Gladders M. D., 2005, *ApJ*, 635, 73
- Hoyle F., 1953, *ApJ*, 118, 513
- Jurić M., Ivezić Ž., Brooks A., et al. 2008, *ApJ*, 673, 864
- Kafle P. R., Sharma S., Lewis G. F., Bland-Hawthorn J., 2012, *ApJ*, 761, 98
- Kafle P. R., Sharma S., Lewis G. F., Bland-Hawthorn J., 2014, *ApJ*, 794, 59
- Kaufmann T., Mayer L., Wadsley J., Stadel J., Moore B., 2007, *MNRAS*, 375, 53
- Kereš D., Katz N., Fardal M., Davé R., Weinberg D. H., 2009, *MNRAS*, 395, 160
- Kereš D., Katz N., Weinberg D. H., Davé R., 2005, *MNRAS*, 363, 2
- Klypin A., Holtzman J., 1997, *ArXiv Astrophysics e-prints*
- Klypin A., Zhao H., Somerville R. S., 2002, *ApJ*, 573, 597
- Kravtsov A. V., 2003, *ApJ*, 590, L1
- Kravtsov A. V., Klypin A. A., Khokhlov A. M., 1997, *ApJS*, 111, 73
- Kravtsov A. V., Nagai D., Vikhlinin A. A., 2005, *ApJ*, 625, 588
- Krumholz M. R., 2015, in Vink J. S., ed., *Astrophysics and Space Science Library* Vol. 412 of *Astrophysics and Space Science Library*, The Formation of Very Massive Stars. p. 43
- Li J.-T., Li Z., Wang Q. D., Irwin J. A., Rossa J., 2008, *MNRAS*, 390, 59
- Licquia T., Newman J., 2014, in *American Astronomical Society Meeting Abstracts #223* Vol. 223 of *American Astronomical Society Meeting Abstracts*, Improved Constraints on the Milky Way Star Formation Rate and Stellar Mass from Hierarchical Bayesian Analysis. p. 336.04
- López-Corredoira M., 2014, *A&A*, 563, A128
- Maller A. H., Dekel A., 2002, *MNRAS*, 335, 487
- Marinacci F., Pakmor R., Springel V., 2014, *MNRAS*, 437, 1750
- Mathews W. G., Brighenti F., 2003, *ARA&A*, 41, 191
- McGaugh S. S., de Blok W. J. G., Schombert J. M., Kuzio de Naray R., Kim J. H., 2007, *ApJ*, 659, 149
- Miller G. E., Scalo J. M., 1979, *ApJS*, 41, 513

- Miller M. J., Bregman J. N., 2013, *ApJ*, 770, 118
- Mo H. J., Mao S., White S. D. M., 1998, *MNRAS*, 295, 319
- Mollitor P., Nezri E., Teyssier R., 2014, *ArXiv e-prints*
- Navarro J. F., Benz W., 1991, *ApJ*, 380, 320
- Navarro J. F., Steinmetz M., 2000, *ApJ*, 528, 607
- Okamoto T., Eke V. R., Frenk C. S., Jenkins A., 2005, *MNRAS*, 363, 1299
- Okamoto T., Jenkins A., Eke V. R., Quilis V., Frenk C. S., 2003, *MNRAS*, 345, 429
- Oman K. A., Navarro J. F., Fattahi A., Frenk C. S., Sawala T., White S. D. M., Bower R., Crain R. A., Furlong M., Schaller M., Schaye J., Theuns T., 2015, *ArXiv e-prints*
- Peebles P. J. E., 1969, *ApJ*, 155, 393
- Pichardo B., Martos M., Moreno E., Espresate J., 2003, *ApJ*, 582, 230
- Piontek F., Steinmetz M., 2011, *MNRAS*, 410, 2625
- Rasheed B., Bahcall N., Bode P., 2010, *ArXiv e-prints*
- Reid M. J., Menten K. M., Brunthaler A., et al. 2014, *ApJ*, 783, 130
- Robertson B., Yoshida N., Springel V., Hernquist L., 2004, *ApJ*, 606, 32
- Robitaille T. P., Whitney B. A., 2010, *ApJ*, 710, L11
- Roca-Fàbrega S., Antoja T., Figueras F., Valenzuela O., Romero-Gómez M., Pichardo B., 2014, *MNRAS*, 440, 1950
- Roca-Fàbrega S., Valenzuela O., Figueras F., Romero-Gómez M., Velázquez H., Antoja T., Pichardo B., 2013, *MNRAS*, 432, 2878
- Scannapieco C., White S. D. M., Springel V., Tissera P. B., 2009, *MNRAS*, 396, 696
- Sofue Y., Honma M., Omodaka T., 2009, *PASJ*, 61, 227
- Stinson G., Seth A., Katz N., Wadsley J., Governato F., Quinn T., 2006, *MNRAS*, 373, 1074
- Stinson G. S., Bailin J., Couchman H., Wadsley J., Shen S., Nickerson S., Brook C., Quinn T., 2010, *MNRAS*, 408, 812
- Stinson G. S., Brook C., Macciò A. V., Wadsley J., Quinn T. R., Couchman H. M. P., 2013, *MNRAS*, 428, 129
- Toft S., Rasmussen J., Sommer-Larsen J., Pedersen K., 2002, *MNRAS*, 335, 799
- White S. D. M., Frenk C. S., 1991, *ApJ*, 379, 52
- White S. D. M., Rees M. J., 1978, *MNRAS*, 183, 341
- Xue X. X., Rix H. W., Zhao G., Re Fiorentin P., Naab T., Steinmetz M., van den Bosch F. C., Beers T. C., Lee Y. S., Bell E. F., Rockosi C., Yanny B., Newberg H., Wilhelm R., Kang X., Smith M. C., Schneider D. P., 2008, *ApJ*, 684, 1143
- Yao Y., Wang Q. D., 2007, *ApJ*, 658, 1088
- Yoachim P., Dalcanton J. J., 2006, *AJ*, 131, 226
- Zemp M., 2013, *ArXiv e-prints*